Received: 15 June 2021 | Revised: 15 October 2021 | Accepted: 28 October 2021

DOI: 10.1111/gcb.15995

PRIMARY RESEARCH ARTICLE

Global Change Biology WILEY

Impacts of the 2012–2015 Californian drought on carbon, water and energy fluxes in the Californian Sierras: Results from an imaging spectrometry-constrained terrestrial biosphere model

Alexander S. Antonarakis[1] | Stacy A. Bogan[2] | Michael L. Goulden[3] | Paul R. Moorcroft[2]

[1]Department of Geography, Sussex University, Brighton, UK

[2]Department of Organismic and Evolutionary Biology, Harvard University, Cambridge, Massachusetts, USA

[3]Department of Earth Sciences, University of California, Irvine, California, USA

Correspondence

Alexander S. Antonarakis, Department of Geography, Sussex University, Chichester 1, Falmer, Brighton BN1 9QJ, UK.
Email: A.Antonarakis@sussex.ac.uk

Paul R. Moorcroft, Department of Organismic and Evolutionary Biology, Harvard University, Cambridge, MA, USA.
Email: paul_moorcroft@harvard.edu

Funding information

National Aeronautics and Space Administration, Grant/Award Number: NNH11ZDA001N-HYSPIRI

Abstract

Accurate descriptions of current ecosystem composition are essential for improving terrestrial biosphere model predictions of how ecosystems are responding to climate variability and change. This study investigates how imaging spectrometry-derived ecosystem composition can constrain and improve terrestrial biosphere model predictions of regional-scale carbon, water and energy fluxes. Incorporating imaging spectrometry-derived composition of five plant functional types (Grasses/Shrubs, Oaks/Western Hardwoods, Western Pines, Fir/Cedar and High-elevation Pines) into the Ecosystem Demography (ED2) terrestrial biosphere model improves predictions of net ecosystem productivity (NEP) and gross primary productivity (GPP) across four flux towers of the Southern Sierra Critical Zone Observatory (SSCZO) spanning a 2250 m elevational gradient in the western Sierra Nevada. NEP and GPP root-mean-square-errors were reduced by 23%–82% and 19%–89%, respectively, and water flux predictions improved at the mid-elevation pine (Soaproot), fir/cedar (P301) and high-elevation pine (Shorthair) flux tower sites, but not at the oak savanna (San Joaquin Experimental Range [SJER]) site. These improvements in carbon and water predictions are similar to those achieved with model initializations using ground-based inventory composition. The imaging spectrometry-constrained ED2 model was then used to predict carbon, water and energy fluxes and above-ground biomass (AGB) dynamics over a 737 km^2 region to gain insight into the regional ecosystem impacts of the 2012–2015 Californian drought. The analysis indicates that the drought reduced regional NEP, GPP and transpiration by 83%, 40% and 33%, respectively, with the largest reductions occurring in the functionally diverse, high basal area mid-elevation forests. This was accompanied by a 54% decline in AGB growth in 2012, followed by a marked increase (823%) in AGB mortality in 2014, reflecting an approximately 10-fold increase in per capita tree mortality from ~55 trees km^{-2} $year^{-1}$ in 2010–2011, to ~535 trees km^{-2} $year^{-1}$ in 2014. These findings illustrate how imaging spectrometry estimates of ecosystem composition can constrain and improve terrestrial biosphere model predictions of regional carbon, water, and energy fluxes, and biomass dynamics.

1 | INTRODUCTION

The response of terrestrial ecosystem dynamics and resulting carbon stocks and fluxes to climate variability and change are one of the largest uncertainties in the Earth's current and future carbon budget (Fisher et al., 2014; Kolus et al., 2019). Due to feedbacks onto atmospheric CO_2 concentrations, these uncertainties regarding the fate of terrestrial ecosystems are the second largest source of uncertainty for the amount of climate predicted in future climate projections (Bodman et al., 2013; Friedlingstein et al., 2014). Reducing these uncertainties hinges on more accurate predictions for the current and future state of terrestrial ecosystems at large scales and improving predictions of ecosystem changes in response to climate change (Ahlström et al., 2012; Friedlingstein et al., 2006; Huntzinger et al., 2012; Michalak et al., 2011).

Californian ecosystems are at threat from climatic changes including prolonged droughts, which are expected to increase (Cook et al., 2015; Swain et al., 2018). Drought events can impact vegetation ecosystems across large spatial scales that are topographically and climatologically diverse (Allen et al., 2010). From 2012 to 2015, California experienced a one in 1000-year drought (Robeson, 2015) leaving the state with a rain debt of around 500 mm equal to a year's rainfall (Cole & Gray, 2015). Multi-year water stress, elevated temperatures and associated insect outbreaks resulted in high canopy water loss and widespread forest mortality (Asner et al., 2016; USFS, 2015; Young et al., 2017). Ecosystems covering the southern Sierra Nevada mountains experienced some of the highest rates of water loss and mortality in the region (Asner et al., 2016; Young et al., 2017). Spanning large elevational gradients, these ecosystems encompass oak savannas, mid-elevation mixed pines, fir and cedar forests and high-elevation pines. Effects of the Californian drought on vegetated ecosystems have mainly been determined using empirical and remote sensing approaches (Asner et al., 2016; Goulden & Bales, 2019; Paz-Kagan et al., 2017; Restaino et al., 2019; Young et al., 2017). However, we have limited understanding of the drought's impact on regional scale carbon, water, and energy fluxes, and biomass dynamics across the region's diverse set of vegetation communities.

The key to improving our understanding of current and future terrestrial carbon, water and energy dynamics is by identification and reduction of three distinct sources of error in terrestrial biosphere model simulations: (i) forcing error, arising from inaccuracies in the meteorological variables used to drive model simulations, (ii) parameterization error, arising from inaccuracies in current parameter values and (iii) initialization error, arising from errors in the description of the current ecosystem state at the beginning of a simulation. Accurate knowledge of the initial or current ecosystem state is crucial when making predictions on timescales ranging from annual to multi-decadal timescales. The traditional approach to conducting terrestrial biosphere model simulations has been to develop a potential vegetation (PV) initial condition, produced via a long-term simulation that begins from a near-bare-ground ecosystem state and force the model with historical meteorology until it reaches near-equilibrium conditions (Heimann et al., 1998; Schaefer et al., 2012; Schwalm et al., 2010). This approach is problematic, however, because the resulting estimated ecosystem state is unlikely to reflect current ecosystem state due to the following: (i) errors in the model formulation and parameters, and (ii) errors and uncertainty in the historical climate forcing and the natural and anthropogenic disturbances experienced by the ecosystem in the past. One alternative is to initialize models with information on current ecosystem composition and structure obtained from ground-based inventories of the plant canopies within small sample plots (e.g. Medvigy et al., 2009; Xu et al., 2016); however, this approach has limited applicability at regional scales (though see Medvigy & Moorcroft, 2012).

Remote sensing technologies are a promising source of regional-scale, spatially consistent current ecosystem composition and structure needed to initialize terrestrial biosphere model simulations (Schimel et al., 2013). With respect to ecosystem structure, research over the past two decades have shown that lidar and radar instruments can provide spatially extensive information on forest canopy height (Dubayah & Drake, 2000; Lefsky et al., 2005), aboveground biomass (Baccini et al., 2012; Saatchi et al., 2007, 2011) and sub-pixel tree density (Antonarakis et al., 2014).

Regarding regional ecosystem composition, over the past decades, a variety of global and regional estimates of ecosystem composition have been produced from multi-spectral satellite imagery, including the following: the 500 m MODIS Land Cover Type 1: International Geosphere-Biosphere Program 'Programme' (Friedl et al., 2010), the 30 m National Land Cover Dataset (NLCD; Homer et al., 2015), the 300 m GlobCover 2009 (Bontemps et al., 2011) and the Global Land Cover-SHARE product (Latham et al., 2014). Many of these products have been created as the basis for defining plant functional types (PFTs) and specifying their spatial distribution within land surface models (Poulter et al., 2015; Sterling & Ducharne, 2008). Two recent studies assessing the impacts of land cover type definitions on ecosystem model predictions found that: (i) incorrect assignment of land cover classes to PFTs, (ii) difficulties in differentiating some vegetation types and (iii) inaccuracies arising from the coarse resolutions of land cover products, were large contributing factors to increased carbon flux uncertainties (Jung et al., 2007; Quaife et al., 2008). Notably, the information offered by current satellite-based products do not adequately resolve important fine-scale heterogeneity in ecosystem composition that is necessary for reducing the error in terrestrial biosphere model simulations.

Forthcoming global-scale imaging spectrometry measurements, which measure surface reflectance in tens to hundreds of contiguous spectral bands, promise to move terrestrial ecosystem monitoring beyond land cover change mapping by providing more resolved information on ecosystem composition (Cawse-Nicholson et al., 2021; Jetz et al., 2012). Imaging spectrometry has the potential of bridging the knowledge gap between coarser land cover types and plant functional diversity, linking functional distributions with climate and environmental change (Jetz et al., 2012). Thus far, work on determining ecosystem composition using imaging spectrometry has primarily relied on airborne platforms, such as the Airborne Visible/Infrared Imaging Spectrometer (AVIRIS), the Compact Airborne

Spectrographic Imager (CASI), the Hyperspectral Mapper (HyMap), the Carnegie Airborne Observatory (CAO), and the Hyperspectral Digital Imagery Collection Experiment (HYDICE). In addition, measurements from the spatially intermittent EO1-Hyperion technology demonstrated instrument have also been used (Goodenough et al., 2003; Kozhoridze et al., 2016; Somers & Asner, 2013). The CAO imaging spectrometer was flown over California recently to estimate forest canopy water loss during the 2012–2015 drought (Asner et al., 2016). Imaging spectrometry-based classifications have been used to identify plant species or PFTs in temperate (Kokaly et al., 2003; Lucas & Carter, 2008; Martin et al., 1998) and tropical ecosystems (Asner & Martin, 2009; Clark et al., 2005; Zhang et al., 2006), and have been shown to produce higher accuracies than multi-spectral sensors (Clark et al., 2005; Goodenough et al., 2003). Recently, Multiple Endmember Spectral Mixture Analysis (MESMA) has been successfully applied in plant species mapping (Dennison & Roberts, 2003a; Roberts et al., 1997, 1998; Roth et al., 2015), with a focus on the heterogeneous ecosystems of California ecosystems (e.g. Dennison & Roberts, 2003b; Roberts et al., 1998; Roth et al., 2012). Since 2013, AVIRIS has been flown over much of California, collecting precursor datasets in advance of NASA's upcoming Surface Biology and Geology (SBG) satellite-based imaging spectrometer mission that will provide a high spatial resolution (30 m) and spectral range (380–2500 nm and 3–12 μm) data capable of providing global-scale information on vegetation composition (Cawse-Nicholson et al., 2021; Lee et al., 2015; NASEM, 2018).

The Ecosystem Demography model (ED2) is a terrestrial biosphere model capable of simulating the carbon, water and energy fluxes of vertically stratified and horizontally heterogeneous plant canopies on timescales of decades to centuries (Longo et al. 2019; Medvigy et al., 2009; Moorcroft et al., 2001). Its ability to represent the fine variation in structure and composition of plant canopies, much of which occurs at the scales of meters—far below the resolution of climatological grid cells—makes it particularly amenable to incorporating information from remote sensing of plant canopies. Studies by Hurtt et al. (2004), Thomas et al. (2008) and Antonarakis et al. (2011) have shown how lidar measurements of canopy structure can be used to improve the model's predictions of carbon flux and dynamics. In a subsequent study, Antonarakis et al. (2014) showed how imaging spectrometry measurements could be used to estimate ecosystem composition at a mixed temperate forest site at Harvard Forest, Massachusetts. This estimate of canopy composition was then combined with a lidar-derived estimate of canopy structure to provide an estimate of above-ground ecosystem state. Incorporating this remote-sensing-derived estimate of above-ground ecosystem state into the ED2 model significantly improved predictions of annual net carbon fluxes, reducing the root-mean squared error (RMSE) from 85% to 104% using PV simulation to 37%–57%.

In this study, we investigate the ability of coarser resolution, but more spatially extensive, imaging spectrometry measurements to provide spatially-resolved estimates of PFT composition suitable for constraining terrestrial biosphere model predictions of carbon, water and energy fluxes. The analysis of Antonarakis et al. (2014) used on high-resolution (6 m) imaging spectrometry measurements to distinguish five PFTs (early- and late-successional conifers, and early-, mid- and late-successional hardwoods) in temperate forest region of ~4 km^2. In this study, we use an AVIRIS-derived 18-m resolution spatially comprehensive estimate of ecosystem composition produced by Bogan et al. (2019) for a ~740 km^2 region in California, using imaging spectrometry measurements collected as part of the NASA HyspIRI preparatory campaign (Hochberg et al., 2015). In contrast to the Antonarakis et al. (2014) analysis, which focused on within-landscape successional diversity, the variation in ecosystem composition and structure analysed in this larger-scale analysis reflects regional-scale variation in composition linked to altitude-driven differences in climate and edaphic variation in soil depth and texture. The purpose of the NASA HyspIRI preparatory campaign is to provide multi-temporal imaging spectrometry data over large areas of California at a spatial resolution approximating the characteristics of anticipated global imaging spectrometry missions, such as the SBG, EnMAP and HISUI (Guanter et al., 2015; Matsunaga et al., 2017; NASEM, 2018).

After evaluating the ability of the imaging-spectrometry-constrained model to predict carbon performance of the model at four flux tower sites, we use the imaging spectrometry-constrained terrestrial biosphere model to explore the impacts of the Californian drought between 2012 and 2015 on regional carbon, water, and energy fluxes, and biomass dynamics across the four principal ecosystems found in the western slopes of the Sierra Nevada; oak savannas, mid-elevation mixed pines, fir–cedar forests and high-elevation pines. This study provides a framework for assimilating near-future global satellite imagery estimates of ecosystem composition with terrestrial biosphere models, constraining and improving their predictions of large-scale ecosystem dynamics and functioning.

2 | METHODOLOGY

2.1 | Study area

The area of investigation is in the southern Sierra Nevada Mountains, northwest of Fresno, California (Figure 1), between elevations of 125 and 3175 meters above sea level. The regional transect is 737 km^2, extending from oak savannas, through to mixed-conifer forests, transiting to high-elevation pines and junipers. The region encompasses the Southern Sierra Critical Zone Observatory (SSCZO) transect that has been investigating ecosystem responses to land-use change and climatic changes. There are four SSCZO flux-towers at different elevation gradients (Figure 1) measuring meteorology and carbon fluxes, with ground-based forest inventories collected in 2014 oriented along the dominant daytime wind direction within a 200 m × 50 m (1 ha). Table 1 provides a summary of characteristics of the four SSCZO flux tower sites. The San Joaquin Experimental Range or SJER (Ameriflux Id US-CZ1; 37.10, −119.73) is the lowest elevation tower at 450 m, with a mean minimum and maximum temperature of 9.3°C and 23.5°C

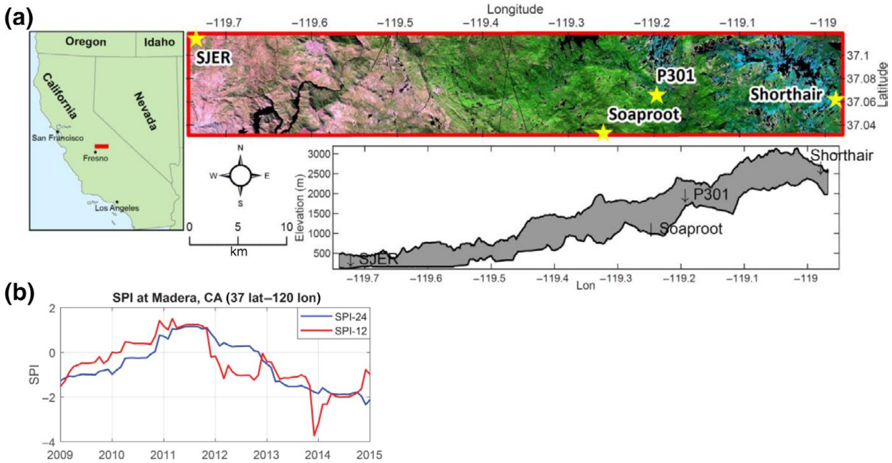

FIGURE 1 (a) Study area box of 11 km by 67 km (737 km^2) over a section of the central Sierra Nevada range in California with the four CZO flux towers identified. The transect shown is a false colour composite of AVIRIS imaging spectrometer data collected in November 2013. Elevation ranges at each longitude are also shown. (b) Standardized precipitation index (SPI) averaged over 24 and 12 months from 2009 to 2015, near the western edge of the study area transect at Madera, California. AVIRIS, Airborne Visible/Infrared Imaging Spectrometer

TABLE 1 Ecosystem characteristics of the SSCZO flux tower sites: San Joaquin Experimental Range (SJER), Soaproot Saddle, P301, and Shorthair Creek

	SJER	Soaproot	P301	Shorthair
Ameriflux ID	US-CZ1	US-CZ2	US-CZ3	US-CZ4
Coordinates	37.10, −119.73	37.03, −119.25	37.06, −119.19	37.06, −118.98
Elevation (m)	450	1160	2015	2700
Temperature range (°C)	9.3–23.5	5.5–18	2.7–14.8	−1.9–10.2
Mean precipitation (mm year^{-1})	510	805	1015	1078
Basal area (m^2 ha^{-1})	5.4	28.9	32.5	43.3
Oak/WhW (%)	84.5	11.1	3.4	0
West Pine (%)	15.5	56.7	10.2	0
Fir/Cedar (%)	0	32.2	82.8	1.1
High Pine (%)	0	0	3.5	98.9

and mean annual precipitation of 510 mm year^{-1}. SJER is an oak savanna ecosystem containing blue oak (*Quercus douglasii*), interior live oak (*Q. wislizeni*), grey pine (*Pinus sabiniana*), California buckeye (*Aesculus californica*), and many species of naturalized and native annual grasses and forbs. The ground-based forest inventory at SJER has as basal area of 5.4 m^2 ha^{-1} with 84.5% oak, and 15.5% grey pine. Soaproot Saddle (Ameriflux Id US-CZ2; 37.03, −119.25) is the second lowest elevation tower at 1160 m, with a mean minimum and maximum temperature of 5.5°C and 18°C and mean annual precipitation of 805 mm year^{-1}. Soaproot is a mixed ponderosa pine (*P. ponderosa*) stand, with oak (*Q. kelloggii* and *Q. chrysolepis*) and incense cedar (*Calocedrus decurrens*) and some white fir (*Abies concolor*). The ground-based forest inventory at Soaproot has as basal area of 28.9 m^2 ha^{-1} with 56.7% ponderosa, 11.1% oak, and 32.2% cedar and fir. The Providence Creek or P301 (Ameriflux Id US-CZ3; 37.06, −119.19) tower is at 2015 m, with a mean minimum and maximum temperature of 2.7°C and 14.8°C and mean annual precipitation of 1015 mm year^{-1}. P301 is a mix of white fir (*A. concolor*), ponderosa pine (*P. ponderosa*), sugar pine (*Pinus lambertiana*), Jeffrey pine (*Pinus jeffreyi*) and incense cedar (*C. decurrens*). The ground-based forest inventory at P301 has as basal area of 32.5 m^2 ha^{-1} with 82.8% fir/cedar, 3.4% oak, 10.2% sugar and ponderosa pine and 3.5% Jeffrey pine. Shorthair Creek (Ameriflux Id US-CZ4; 37.06, −118.98) is the highest elevation tower at 2700 m, with a mean minimum and maximum temperature of −1.9°C and 10.2°C and mean annual precipitation of 1078 mm year^{-1}. Shorthair is in the subalpine belt of the Sierra Nevada and is comprised mostly of lodgepole pine (*P. contorta*) and western white pine (*P. monticola*), with around 1% of the area occupied by red fir (*Abies magnifica*) and has a basal area of 43.3 m^2 ha^{-1}. Size class distributions at the four flux tower sites resulting from ground-based forest composition and structure are shown in Figure 2 (top row).

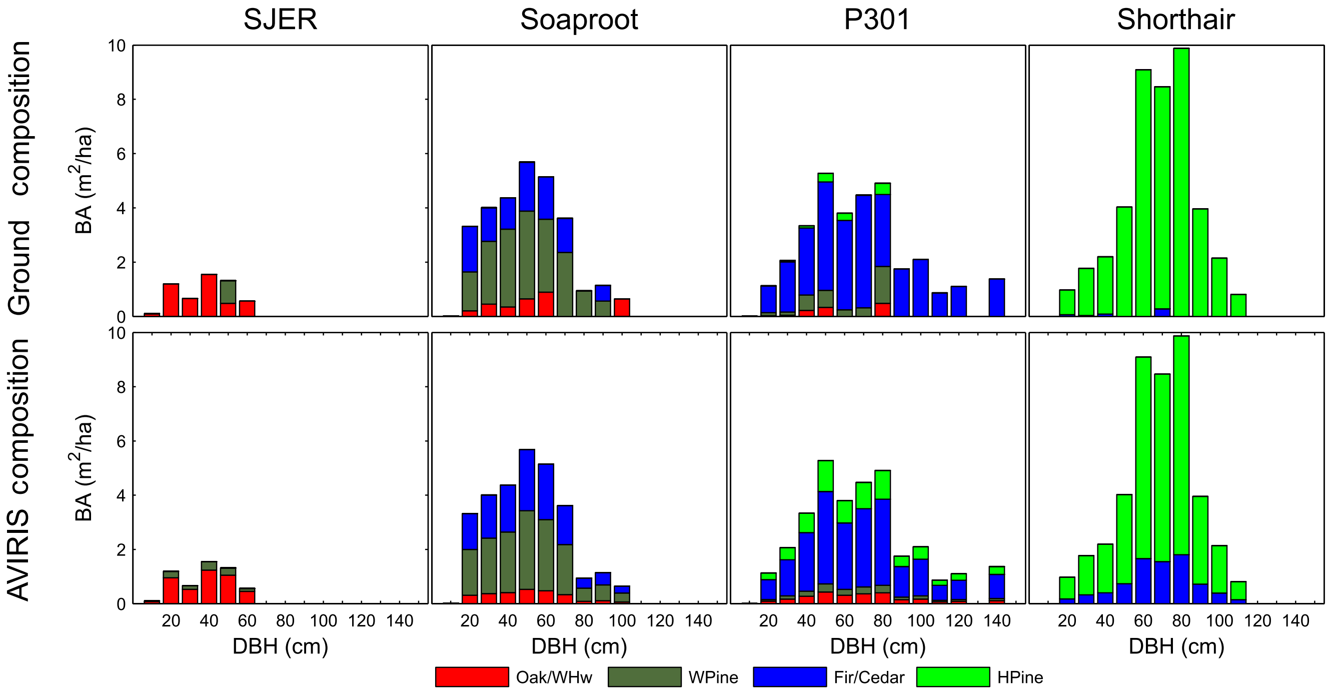

FIGURE 2 Basal area (BA) size class distributions at the four flux tower sites (SJER, Soaproot, P301, Shorthair) showing the ground-inventory canopy composition estimate (top row) and the AVIRIS-derived composition estimates (bottom row). The ground-inventory BA composition of Oaks and Western Hardwoods (Oak/WHw), Western Pines (WPine), Firs and Cedars (Fir/Cedar) and High Pines (HPine) were 84.5/15.5/0/0% for SJER, 11.1/56.7/32.2/0% for Soaproot, 3.4/10.2/82.8/3.5% for P301, and 0/0/1.1/98.9% for Shorthair. The corresponding AVIRIS Imaging spectrometry-derived composition estimates were 79.7/20.3/0/0% for SJER, 9.3/51/39.7/0% for Soaproot, 8.1/5.6/64.7/21.6% for P301, 0/0/18.3/81.7% for Shorthair. Note that the imaging spectrometry-derived fractional composition is applied uniformly across the size classes. AVIRIS, Airborne Visible/Infrared Imaging Spectrometer; SJER, San Joaquin Experimental Range

2.2 | ED2 terrestrial biosphere model

The ED2 model is an integrated terrestrial biosphere model calculating the exchange of carbon, water and energy, incorporating hydrology, land-surface biophysics, vegetation dynamics and soil carbon and nitrogen biogeochemistry (Longo et al., 2019; Medvigy et al., 2009; Moorcroft et al., 2001). ED2 uses a set of size- and age-structured partial differential equations that track the changes in abundance of plants of different sizes and PFTs arising from plant growth, mortality, recruitment and the impact of disturbances. ED2 is able to realistically represent the dynamics of spatially heterogeneous plant communities incorporating the effects of natural disturbance processes such as fire, and anthropogenic disturbances such as forest harvesting or land clearing and climatic changes (e.g. Albani et al., 2006; Hurtt et al., 2004; Medvigy et al., 2009; Zhang et al., 2015).

In the ED2 model, a given simulation region is subdivided into a series of climatological grid cells that experience the same meteorological forcing, which is specified from meteorological observations, climate reanalysis datasets, or from the boundary conditions of an atmospheric model. Each climatological grid cell is subdivided into a number of horizontal tiles representing areas of forest that share a similar vegetation canopy structure and disturbance history. The state of the above ground ecosystem is described within each tile ($n^i(z,a)$) by the density (n) of individual trees of different sizes (z), for a series of PFTs (i), and time (a) since last disturbance. The different PFTs differ in terms of their eco-physiological and morphological traits that result in different rates of growth and mortality and sensitivity to environmental conditions. The ecophysiology and allometric parameters of the five PFTs represented in this study are presented in Table 2. The description of the above-ground ecosystem state embodied in the ED2 model allows for realistic projections of both the fast-timescale exchanges of carbon, water and energy between the land and the atmosphere, and long-term vegetation dynamics. Further details on the description of plant physiology, decomposition and water stress in ED2 are given in Appendix 1.

2.3 | Ecosystem composition derived from imaging spectrometry

Above-ground canopy composition in the ED2 model is represented by a series of PFTs that have different biophysical, physiological, morphological and ecological properties. In this study (see Table 2), the vegetation community was considered a mixture of five PFTs assigned as Oaks and Western Hardwoods (e.g. *Q. douglasii*, *Q. wislizeni*, *A. californica*), Western Pines (e.g. *P. sabiniana*, *P. ponderosa*), Firs and Cedars (e.g. *A. magnifica*, *A. concolor*, *C. decurrens*), High-elevation Pines (sub-alpine species e.g. *P. contorta*, *P. jeffreyi*, *P. monticola*) and Grasses/Shrubs.

TABLE 2 California plant functional type eco-physiology, allometric parameters, and species

Property	Oak/WhW	West Pine	Fir/Cedar	High Pine	Grass	Literature
V_{m0} (μmol $m^{-2}s^{-1}$)	30	10	10	7	15	Xu and Baldocchi (2003), Bond et al. (1999), Manter and Kerrigan (2004), Monson et al. (2005)
Stomatal slope (M)	8.88	10	9	6	9	Xu and Baldocchi (2003), Misson et al. (2004)
Cuticular conductance (μmol $m^{-2}s^{-1}$)	6000	1000	10000	1000	20,000	Xu and Baldocchi (2003), Misson et al. (2004), Warren et al. (2004)
Water conductance (m^2/s/kg_C_root)	400	100	100	100	400	
Leaf turnover rate (a^{-1})	-	0.25	0.25	0.18	2	Law et al. (2001), Balster and Marshall (2000), Miller and Urban (1999), Coops and Waring (2011)
Fine root turnover rate (a^{-1})	1	0.53	0.5	0.18	2	Campbell et al. (2009), Tingey et al. (2005), Gill and Jackson (2000), Coops and Waring (2011)
SLA (m^2 kg^{-1})	10	8	6	7	22	Xu and Baldocchi (2003), Bond et al. (1999), Miller and Urban (1999) Medvigy et al. (2009); Berner and Law (2016)
Fine roots to leaves allocation ratio (kg_fine_roots/kg_leaves)	1.6	0.75	0.355	0.6	1.0	Millikin and Bledsoe (1999), Karlik and McKay (2002), Law et al. (2003), Bartelink (1998)
DBH -height allometry slope	−0.023	−0.0055	−0.0065	−0.0128	$f(B_{leaf})$	FIA data
DBH-height allometry intercept (m)	14	90	80	44.8	$f(B_{leaf})$	FIA data
DBH-leaf allometry slope	1.455	1.8215	1.5489	1.8369	1.0	Ter-Mikaelian and Korzukhin (1997), Jenkins et al. (2003), Chojnacky et al. (2014)
DBH-leaf allometry intercept (kg leaf biomass plant)	0.087	0.0458	0.1272	0.0478	0.08	Ter-Mikaelian and Korzukhin (1997), Jenkins et al. (2003), Chojnacky et al. (2014)
DBH-stem allometry slope	2.4572	2.238	2.5951	2.6747	0	Ter-Mikaelian and Korzukhin (1997), Jenkins et al. (2003), Chojnacky et al. (2014)
DBH-stem allometry intercept (kg stem biomass/plant)	0.1617	0.147	0.075	0.0364	0	Ter-Mikaelian and Korzukhin (1997), Jenkins et al. (2003), Chojnacky et al. (2014)

Plant functional types	Species
Oak/West Hardwood	*Quercus kelloggii, Q. douglasii, Q. chrysolepis, Q. wislizeni, Acer macrophyllum, Platanus racemosa, Aesculus californica, Alnus rhombifolia*
West Pine	*Pinus sabiniana, P. lambertiana, P. ponderosa, P. attenuata*
Fir/Cedar	*Abies magnifica, A. concolor, Calocedrus decurrens, Pseudotsuga menziesii*
High Pine	*Pinus contorta, P. albicaulis, P. jeffreyi, P. monticola, P. monophylla, Juniperus* spp.

Abbreviations: DBH, diameter at breast height; FIA, forest inventory and analysis; SLA, specific leaf area.

The relative abundance of these PFTs was estimated using AVIRIS imaging spectrometry, described in detail in a recent paper (Bogan et al., 2019). The methodology is briefly summarized below. AVIRIS data with an 18 m spatial resolution, were flown over the SSCZO area over two dates, June 12 and November 5 2013. The AVIRIS data were received as surface reflectance from the Jet Propulsion Laboratory, and had undergone ortho-rectification, radiometric and atmospheric correction (Thompson et al., 2015); however, a bidirectional reflection distribution function correction was not applied. Individual AVIRIS flight-lines were mosaicked, subset to the study area (Figure 1), and bands were reduced from 224 to 167 removing streaky, inconsistently dark and inconsistently bright bands, yielding a data set covering three portions of the electromagnetic spectrum: 443–1342 nm, 1422–1790 nm, and 2106–2405 nm. These final bands from the two dates were stacked together resulting in 334 bands. The relative abundance composition of the different PFTs was then determined from AVIRIS using Roberts et al.'s (1998) MESMA algorithm, which estimates the fractional abundances of the different vegetation types and/or land cover types within each 18 m pixel. Areas of the image that were urban, agriculture, barren, or water were masked out prior to the MESMA analysis. An end-member spectral library was generated by taking samples from the AVIRIS image for species associated with each PFT (see Table 2). The spectral libraries were created first by taking samples in areas where target species dominated using ground knowledge of where these dominant species were located, or aided by CALVEG (Classification and Assessment with Landsat of Visible Ecological Groupings; CALVEG, 2010) plant associations that had clear distinctions in PFTs (e.g. oaks and pines or pines, cedar, and fir), but not in associations that were highly mixed, such as mixed-conifer pine. The CALVEG data set is comprised of polygons (average size 0.026 km^2) categorized into plant associations produced by the US Forest Service using a combination of Landsat, field verification and expert guidance. Each CALVEG plant association contains a list of plant species, but their relative abundances are not provided. Then, high-resolution (30 cm–60 cm) satellite and aerial imagery from World Imagery in ArcGIS (sources: ESRI, DigitalGlobe, GeoEye, i-cubed, USDA FSA, USGS, AEX, Getmappint, Aerogrid, IGN, IGP, Swisstopo and the GIS User Community) was used to identify areas that were densely vegetated and contained high canopy cover of a target PFT, to diminish the influence of ground reflectance when creating the spectral libraries for the PFTs. In addition to vegetation signatures, a background class comprising rock and soil spectral signatures were also collected in areas of bare soil and exposed rock in mountainous areas aided by high-resolution imagery. Overall, 199 end-members were sampled over an area of 388,000 m^2, averaging 9–26 end-members over 49,000 m^2 per PFT.

In Bogan et al.'s (2019) MESMA classification that was used in this study, not all spectral end-members were used in each pixel: only PFTs indicated by the CALVEG association for a given pixel were included in the MEMSA calculation for the pixel. For example, for a pixel belonging to the Mixed Conifer-Fir CALVEG association, end-members for the Western Pine, Fir/Cedar and High-elevation Pine PFTs were evaluated, but not Western Hardwoods and Grasses/Shrub end-members. The resulting AVIRIS-based estimates of ecosystem composition for all four Sierra Nevada CZO flux tower sites are shown in Figure 2 (bottom row) and are compared with ground-based composition (Figure 2 top row), with resulting errors at the four flux towers of 3.5% for Oaks/Western Hardwoods, 4.4% for Western Pine, 13% for Fir-Cedar, and 12.5% for High Pine. Independent evaluation of the sub-pixel canopy composition estimates against 95 ground-inventory plots indicated a high level of accuracy in the composition estimates with average RMSEs of 11.3% (see Bogan et al., 2019 for further details).

2.4 | Predictions of carbon, water and energy fluxes, and vegetation dynamics

The AVIRIS-based estimates of ecosystem composition were used to initialize a series of ED2 terrestrial biosphere model simulations at the four flux towers and for the 737 km^2 region. Site-level simulations were conducted for the periods 2010–2014, 2009–2014, 2010–2014 and 2010–2011 at the SJER, Soaproot, P301, Shorthair tower sites, respectively. This variable simulation period was due to available observed meteorological forcing measuring air temperature, precipitation, relative humidity, wind, pressure and radiation at 30-min intervals. The site-level simulations were conducted using three different sources of information for the canopy composition and structure at the beginning of the simulation period (see initial condition descriptions in Section 2.5): (i) ecosystem structure and composition prescribed from the output of a conventional, long-term equilibrium PV simulation; (ii) ecosystem structure and composition prescribed from ground-based inventory measurements; and (iii) ecosystem composition prescribed from imaging spectrometry measurements but with structure prescribed from ground-based measurements.

Regional-level simulations were conducted for the period 2009–2014 for the 737 km^2 region of the lower Sierra Nevada Mountains (Figure 1). The ecosystem composition at the beginning of the simulation period is based on imaging spectrometry composition estimates, and the structure is based on spatially extrapolating US forest service's Forest Inventory and Analysis (FIA) plots. A flowchart describing the inputs, forcings and initial conditions needed to conduct ED2 simulations is shown in Figure 3. Regional meteorological forcing encompassing hourly over-canopy air temperature, downward shortwave and longwave radiation, precipitation, specific humidity, wind velocities and surface air pressure were obtained from the North American Land Data Assimilation Version 2 (NLDAS-2) with a spatial resolution of 1/8° (Mitchell et al., 2004). Soil depth to bedrock and soil texture was obtained from the SSURGO database (NRCS, 2017). Leaf phenology for deciduous woodland (i.e. Oak/West Hardwoods) was prescribed using MODIS (Zhang et al., 2003). This is based on fitting logistic functions to points of inflection constituting dates for green-up, maturity, senescence and dormancy of leaves. Note that all forest types at a location were assumed to

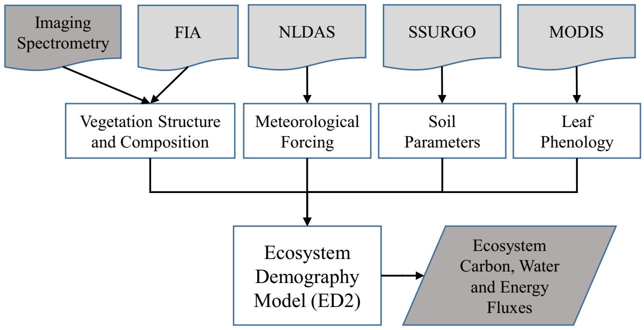

FIGURE 3 Flowchart describing the inputs, forcings and initial conditions needed to produce ecosystem carbon, water and energy flux estimates from the ED2 model [Colour figure can be viewed at wileyonlinelibrary.com]

experience the same climate forcing and all simulations have the same model parameterization. The observed and NLDAS meteorological monthly precipitation and mean temperature at each site is shown in Figure S1.

Site-level carbon, water, energy fluxes and regional-level carbon, water, energy fluxes and vegetation dynamics are predicted in this study, encompassing the majority of the Californian drought from 2012 to 2015. Details on ED2 model predictions of carbon, water, and energy fluxes are given in Appendix 1. Site-level carbon and water predictions of net ecosystem productivity (NEP), gross primary productivity (GPP), and evapotranspiration (ET) from the three site-level simulation types are compared against each other, and to observed patterns from each flux tower. At the regional-level, carbon fluxes are also quantified as NEP and GPP, water fluxes are quantified as evaporation and transpiration, and energy fluxes are quantified as canopy latent and sensible heat. Vegetation dynamics are also predicted and quantified in this study as yearly above-ground-biomass growth and mortality.

2.5 | Integrating ecosystem composition into the ED2 biosphere model

2.5.1 | Site-level analysis

To initialize the ED2 model, cohort level tree size, density and PFT information specifying the sub-grid scale tiles spatial variation in canopy structure, is required. In the PV simulations this information is obtained by initializing the ED2 model with a near bare-ground condition and running the model for 300 years yielding an ecosystem structure and composition that is in dynamic equilibrium with the climate-forcing data at each of the four SSCZO sites. The PV simulations resulted in basal areas of 29.6, 76.8, 68.0, 75.1 m^2 ha^{-1} for SJER, Soaproot, P301 and Shorthair, respectively, and consisted of 95%, 99%, 90%, 90% Fir-Cedars with the remainder Western Pines. Size class distributions of the PV runs at the four flux towers are provided in Figure S2.

The second site-level simulations were initialized from *ground-based forest inventory measurements* at each of the four SSCZO flux tower sites. These measurements come from a 1 ha forest inventory plot located in the tower footprint at each flux tower site. Each forest inventory plot is comprised of sixteen 25 m × 25 m sub-plots organized in a spatially contiguous 2-by-8 array oriented along the dominant daytime wind direction at each flux-tower site (Kelly, 2014). Following the approach of Medvigy et al. (2009) and Antonarakis et al. (2014), the flux-tower footprint was represented as a collection of 16 tiles corresponding to the 16 forest inventory sub-plots at each SSCZO site, with each tile containing trees of different size and stem densities and PFT composition, thereby representing the observed horizontal heterogeneity in canopy composition and structure. An initial understory grass layer within each existing tile or sub-plot at SJER was added with an leaf area index (LAI) of 1 m^2 m^{-2} (Xu et al., 2004); however, grasses reach an equilibrium with the climate forcing within the first years of simulation. For all sites, each tree species was assigned a PFT following the classification shown in Table 2. Initial levels of soil carbon pools were prescribed as 2.55 kgC m^{-2} for the upland forested sites (Southern Sierra CZO, 2012), and 2.8 kgC m^{-2} for SJER (Schnabel et al., 2013). Soil depth and soil texture was obtained from the SSURGO database, with depths of 1.5 m for SJER and P301, and 2 m for Soaproot and Shorthair, and all sites dominated by sandy soils (between 67% and 78% sand for all sites).

The third site level simulations used *ecosystem composition* derived from AVIRIS imaging spectrometry described in the previous Section 2.3. For these site level simulations, the remote-sensing derived estimate of ecosystem composition over the 1-ha forest inventory plots located within the footprint of each tower site, was used to specify ecosystem composition. Following Antonarakis et al. (2014), the normalized abundances (q) of the four woody PFTs (i) were applied consistently across all tree sizes to obtain the initial tree density:

$$n^i\left(z,x,t_o\right) = n_{\text{ground}}\left(z,x\right) * q^i\left(x\right) \tag{1}$$

Here, the ground inventory tree density as a function of trunk diameter ($n_{\text{ground}}(z)$) in tile x is scaled by the PFT abundance ($q^i(x)$) derived from imaging spectrometry. Size class distributions from ground-based inventories, and from the composition adjustment are shown in Figure 2.

2.5.2 | Regional-level analysis

The imaging spectrometry-derived estimate of regional ecosystem composition from Bogan et al. (2019) was subsequently used to prescribe the composition of the above-ground ecosystem across the 737 km^2 simulation domain. The regional simulations were conducted on a 1 km^2 grid. This resolution was chosen because of the relatively coarse spatial resolution of available regional meteorological forcing data (spatial resolution of 1/8°, see above) and soil texture and forest structure data (see below).

Soil depth and soil texture were obtained from the SSURGO database in vector-based format (see Figure S3 for the SSURGO soil data for the simulation region). Information on the spatial variation in forest structure across the region was prescribed from measurements from US forest service's FIA program that has an extensive network of plots across the United States. Each FIA plot consists of four 14.2 m diameter sub-plots located within a 0.4-ha area, in which diameter measurements are taken on individual stems greater than one inch in diameter and identified to species. Estimates of soil carbon are also available for all plots. Within the study region, 30 FIA plots were available with data on trunk diameters per area and soil organic carbon. These were used to prescribe forest structure across the 737 km^2 region, by stratifying the plots into 250 m elevation bins using the National Elevation Dataset (NED). The FIA plots falling into a given 250 m elevation bin were then used to specify the size-structure of the above-ground ecosystem within the series of 1 km^2 climatological grid-cell within the corresponding elevation range. Two extra sub-grid tiles are added for each climatological grid-cell (x) at initialization (t_o) with a representative grass/shrub layer and near bare-ground tiles. Mathematically, this corresponds to the following:

$$p_{\mathrm{FR}}^{f}\left(a,x,t_{\mathrm{o}}\right) = \frac{Q_{\mathrm{FR}}(x)}{N} * p_{\mathrm{FIA}}^{f}(a,x) \quad (f = 1 \cdots N)$$

$$p_{\mathrm{GR}}^{N+1}\left(a,x,t_{\mathrm{o}}\right) = Q_{\mathrm{GR}}(x) * p_{\mathrm{GR}}(a)$$

$$p_{\mathrm{BG}}^{N+2}\left(a,x,t_{\mathrm{o}}\right) = Q_{\mathrm{BG}}(x) * p_{\mathrm{seedlings}}(a) \tag{2}$$

That is, the FIA forest tiles, and new tiles created for grasses and bare-ground are adjusted by the fractional composition of forest ($Q_{\mathrm{FR}}(x)$), grass/shrub ($Q_{\mathrm{GR}}(x)$) and bare-ground ($Q_{\mathrm{BG}}(x)$). N is the total number of forest tiles from FIA and the superscript f denotes the individual forest tiles ($f = 1 \ldots N$). The fractional cover of forest, grass/shrub and bare-ground are specified from the imaging spectrometry-derived estimate of regional ecosystem composition, where the forest fraction is the sum of the classified woody PFTs across each 1-km grid cell. As in the site-level imaging spectrometry-initialized simulations (Equation 1), the relative abundances of the different tree cohorts of a forest tile within each 1-km grid cell were calculated using in a similar manner to Equation (1), that is, multiplying the FIA forest-inventory-derived stem density information by the fractional abundance of each PFT for each 1-km grid cell. The near bare-ground tile ($p_{\mathrm{seedlings}}(a)$) was populated with seedlings of all ED2 PFTs. Because there is currently no parameterization for shrubs in ED2, all shrubs classified from imaging spectrometry were combined into a grass/shrub tile ($p_{\mathrm{GR}}(a)$) populated with LAI values using the LAI estimate from the nearest grass-shrub dominated MODIS pixel where the MESMA-derived grass/shrub class dominated (>75%). As for the site level runs, the grasses come into equilibrium within the first few years of simulation. The final regional estimates of ecosystem composition and structure used to initialize the ED2 model over the 737 km^2 transect in the Sierra Nevada are shown in Figure 4.

3 | RESULTS

3.1 | Site-level analysis

3.1.1 | Carbon flux predictions

The ED2 model predictions of seasonal carbon fluxes at the four flux tower sites are shown in Figure 5. Improvements in carbon flux estimates arising from the remote-sensing initializations were assessed by comparing the predictions from the AVIRIS-initialized simulations to the predictions obtained from PV-initialized simulations and from ground-inventory initialized simulations. The PV-initialized simulation predicted seasonal GPP at SJER, Soaproot, P301 and Shorthair with RMSEs of 0.032, 0.081, 0.059, 0.11, respectively, kgCm^{-2} month^{-1} (see Table 3). Compared with observed fluxes, the

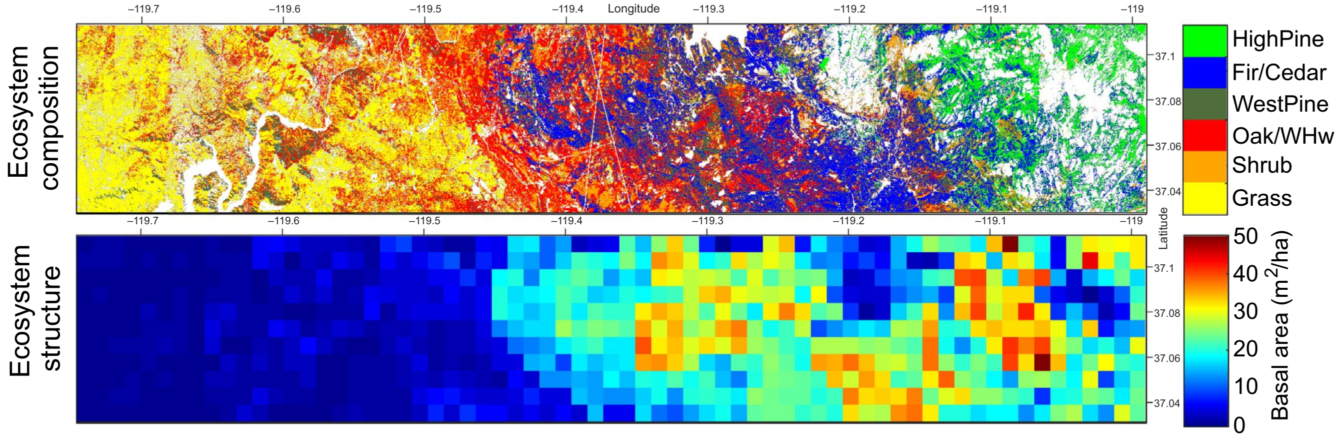

FIGURE 4 Regional ecosystem structure expressed in terms of basal area (m^2/ha) in 1 km pixels derived from the USFS Forest Inventory and Analysis dataset, and Ecosystem Composition derived from 18-m resolution AVIRIS imaging spectrometry flown in 2013. Masked (white) pixels in the top panel are both barren/rock surfaces as well as water bodies. AVIRIS, Airborne Visible/Infrared Imaging Spectrometer

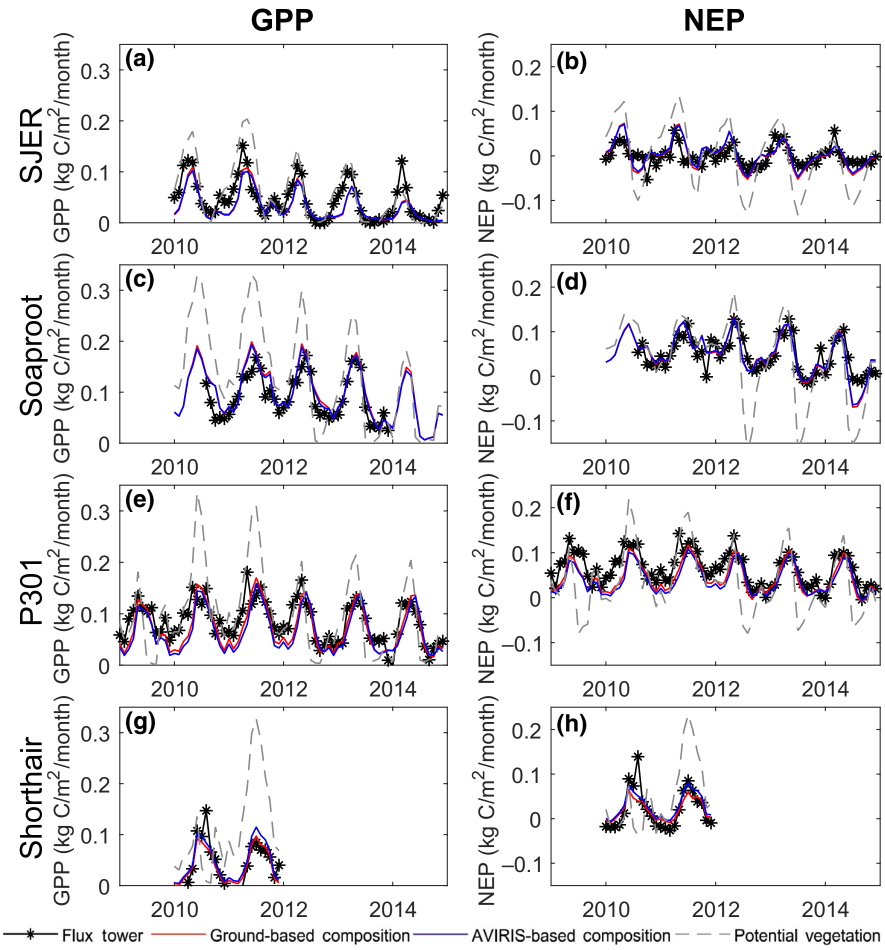

FIGURE 5 Predicted versus observed seasonal gross primary productivity (GPP) and net ecosystem productivity (NEP) at the four flux tower evaluation sites; SJER (a, b), Soaproot (c, d), P301 (e, f) and Shorthair (g, h). Black lines and points show the observed fluxes; remaining lines show the predictions of the ED2 terrestrial biosphere model when initialized with: ground-based estimates of canopy composition (red lines); AVIRIS-based estimates of canopy composition (blue lines) and canopy composition estimated from an equilibrium potential vegetation simulation (grey dashed lines). AVIRIS, Airborne Visible/Infrared Imaging Spectrometer; SJER, San Joaquin Experimental Range

PV-initialized simulations (grey dashed lines) over-estimated the magnitude of GPP seasonality at the SJER, Soaproot and P301 flux tower sites (see Figure 5a,c,e). The degree of over-estimation was highest during the pre-drought period (2010–2011) and declined following the onset of the drought in 2012. At Shorthair flux tower site, the degree of GPP seasonality was too low in 2010 and elevated throughout 2011. In addition, the seasonal timing of GPP in 2010 was poorly captured with too low carbon fluxes during the summer and too high during the winter and autumn months (Figure 5g).

Compared with the PV-initialized simulations, the ground-based initialized simulation predictions of seasonal GPP more closely match the observed fluxes at all four evaluation sites (Figure 5a,c,e,g, red lines). The ground-based initialized simulations predicted seasonal GPP at SJER, Soaproot, P301, and Shorthair with RMSEs of 0.026, 0.025, 0.028 and 0.019 kgC m^{-2} month^{-1}, representing reductions of 19%, 69%, 51% and 83%, respectively, in RMSEs compared with the PV-initialized simulation (Table 3). Similar to the ground inventory-initialized simulations, the AVIRIS-initialized predictions of GPP also more closely match the observations than the PV-initialized simulations at the four flux tower sites (Figure 5a,c,e,g, blue lines). The AVIRIS-initialized seasonal carbon flux predictions (blue lines) closely follow that of the ground inventory-initialized simulations (red lines) across all four sites and consequently exhibit similar improvements in accuracy over the PV-initialized simulations: the AVIRIS-initialized predictions had RMSEs of 0.026, 0.023, 0.034, 0.021 kgC m^{-2} month^{-1} at SJER, Soaproot, P301 and Shorthair, respectively, reductions of 19%, 72%, 42% and 82% over the PV-initialized simulations (Table 3).

The PV-initialized simulations predicted the observed seasonal patterns of NEP with RMSEs of 0.059, 0.071, 0.060 and 0.078 kgC m^{-2} month^{-1} (see grey dashed lines in Figure 5b,d,f,h; Table 3). At SJER and P301, the PV-initialized simulation overestimated NEP during the winter and spring months, and underestimated NEP during the summer (Figure 5b,f). At Soaproot, the PV-initialized NEP predictions were relatively consistent with the observations during 2010 and 2011 (Figure 5d), while at Shorthair the predictions were too low in 2010 and too high in 2011 (Figure 5h). At SJER, Soaproot and P301, the three sites where the measurements extended into the drought period (2012–2014), the PV-initialized predictions of NEP declined at Soaproot and P301 and the seasonality of NEP increased following the onset of the drought; however, the declines were larger than observed particularly during summer months.

The ground-inventory initialized simulations predicted observed seasonal NEP at SJER, Soaproot, P301 and Shorthair with RMSEs of 0.022, 0.026, 0.028 and 0.026 kgC m^{-2} month^{-1}, with reductions of 63%, 64%, 54% and 67% in the RMSEs at the four sites compared PV-initialized simulations. Several mismatches remain, however, including lower-than-observed springtime NEP during 2014 at SJER; lower-than-observed wintertime NEP in 2010 and 2012 at P301; and lower-than-observed summer-time NEP in 2014 at Soaproot. However, the ground-based initialized simulations more clearly capture the observed decreases in GPP and NEP that were observed at SJER, Soaproot and P301 flux tower sites following the onset of drought period (2012–2014) (Figure 5, compare red and black lines). Similarly, with respect to NEP, the AVIRIS-initialized predictions at SJER, Soaproot, P301 and Shorthair has RMSEs of 0.021, 0.025, 0.033 and 0.024 kgC m^{-2} $month^{-1}$, 64%, 64%, 46% and 69% reductions, respectively, in RMSEs compared with PV-initialized predictions.

The predictions of annual carbon fluxes at the four flux towers are shown in Figure 6. The observed yearly mean GPP values at SJER, Soaproot, P301 and Shorthair (Figure 6a) were 0.55, 1.13, 1.02 and 0.48 kgC m^{-2} $year^{-1}$, respectively (Figure 6a). The PV simulations (Figure 6b) predicted higher annual GPP at all sites with up to three times more inter-annual variability at SJER, Soaproot and P301, and 14 times more variability at Shorthair. The PV simulations predicted the observed annual GPP fluxes with RMSEs of 0.25, 0.67, 0.35 and 1.10 kgC m^{-2} $year^{-1}$ at SJER, Soaproot, P301 and Shorthair, respectively (Figure 6b). As with the seasonal carbon fluxes, both ground inventory-initialized and AVIRIS-initialized predictions of annual average GPP more closely match the observed fluxes with more accurate prediction of both the mean annual uptake and more accurate levels of inter-annual variability at all four evaluation sites (Figure 6c,d). The ground inventory-initialized simulations predicted annual GPP at SJER, Soaproot, P301 and Shorthair with RMSEs of 0.18, 0.14, 0.19 and 0.07 kgC m^{-2} $year^{-1}$, respectively, representing 29%, 79%, 46% and 94% reductions in RMSEs compared with the PV-initialized model predictions. Similarly, the AVIRIS-initialized simulations predicted annual GPP at SJER, Soaproot, P301 and Shorthair with RMSEs of 0.18, 0.11, 0.26 and 0.12 kgC m^{-2} $year^{-1}$, respectively, representing 27%, 83%, 24% and 89% reductions in RMSE compared with the PV-initialized simulations.

The observed yearly mean NEP values at SJER, Soaproot, P301, and Shorthair (Figure 6e) were −0.0025, 0.58, 0.77, and 0.25 kgC m^{-2} $year^{-1}$, respectively, indicating that, over their respective observation periods, SJER was essentially carbon neutral, Soaproot and P301 were significant carbon sinks, and Shorthair was a moderate carbon sink. With respect to NEP, the PV simulations at SJER, Soaproot and P301 predicted lower-than-observed average annual NEP with up to five times more inter-annual variability than observed fluxes, whereas at Shorthair the PV simulations had higher-than-observed average NEP and 13 times more inter-annual variability than the observed fluxes (Figure 6f) and with RMSEs of 0.27, 0.40, 0.41 and 0.66 kgC m^{-2} $year^{-1}$ at the SJER, Soaproot, P301 and Shorthair sites, respectively (Table 3). Similar to the annual GPP predictions, both ground-initialized and AVIRIS-initialized predictions of annual average NEP more closely match the observed fluxes with more accurate prediction of both mean annual uptake, and more accurate levels of inter-annual variability at all four evaluation sites (Figure 6g,h). The ground-inventory initialized simulations predicted annual NEPs at SJER, Soaproot, P301, and Shorthair with RMSEs of 0.11, 0.10, 0.25 and 0.05 kgC m^{-2} $year^{-1}$, representing 59%, 74%, 39% and 93% reductions in RMSEs compared with the PV-initialized predictions (see Table 3); in a similar manner, AVIRIS-initialized predictions of annual NEP had RMSEs of 0.11, 0.09, 0.32 and 0.12 kgC m^{-2} $year^{-1}$ at SJER, Soaproot, P301 and Shorthair, respectively, representing reductions of RMSEs of 58%, 76%, 23% and 82% compared with the PV-initialized model predictions (see Table 3).

3.1.2 | Water flux predictions

The ED2 model predictions of seasonal ET for the period 2009–2014 are shown in Figure 7. At SJER (Figure 7a) the observed seasonal ET (black lines) is highest during the winter and spring, while at Soaproot, SJER and Shorthair (Figure 7b–d), ET is highest during the spring and summer. Although data are not available at Shorthair, as seen in Figure7b–d, after 2012 there are noticeable declines in seasonal ET at SJER, Soaproot and P301. The seasonal patterns of ET predicted by the PV-initialized simulation (grey dashed lines in Figure 7) show similar seasonal patterns to the observations; however, the model significantly over-estimates ET at SJER in 2011 (Figure 7a) and Soaproot in 2011 (Figure 7d), and under-estimates ET at Soaproot and P301 in 2012 and 2013 (Figure 7b,c). The predicted peak values are generally lower-than-observed at P301 and higher-than-observed at SJER; however, the PV-initialized simulation captures the observed decreases in ET at SJER, Soaproot and P301 that occur during 2012–2014. At Shorthair (Figure 7d), the ET predictions from PV-initialized simulation are more variable seasonally than the observed fluxes, and the temporal trend is also different: the observed fluxes decrease from 2010 to 2011, whereas the PV-initialized fluxes increase for the same period. The RMSEs of the PV-initialized runs were 19, 23, 32 and 42 mm H_2O $month^{-1}$ at SJER, Soaproot, P301 and Shorthair, respectively (see Table 3).

Ground-based and AVIRIS-based initialized predictions of ET (red and blue lines in Figure 7a–d) are very closely aligned and follow similar seasonality as the observed water fluxes: the highest water fluxes occur during the winter and spring at SJER, and during the spring and summer at Soaproot, SJER and Shorthair, and the predictions capture the observed decreases in seasonal ET that occur after 2012 at SJER, Soaproot and P301. The ground-initialized and AVIRIS-initialized simulations had minor overall improvements in the predictions of water fluxes: the ground-initialized simulations yielded RMSEs of 19, 21, 24, 29 mm H_2O $month^{-1}$ at SJER, Soaproot, P301 and Shorthair, respectively, representing 0%, 11%, 26% and 31% reductions in RMSEs compared with the PV-initialized simulations. The AVIRIS-initialized predictions of ET had RMSEs of 20, 21, 24 and 34 mm H_2O $month^{-1}$ at SJER, Soaproot, P301, and Shorthair, respectively, representing a 4% increase in RMSE at SJER, and reductions of 9%, 23% and 19% in RMSEs at Soaproot, P301 and Shorthair compared with the PV-initialized simulations. However,

TABLE 3 Seasonal and annual GPP, NEP and ET RMSEs derived from potential vegetation (PV), ground-based, and AVIRIS-based initialized simulations, compared to flux tower observed fluxes (OBS)

Seasonal fluxes	GPP (kgC m^{-2} month^{-1})				NEP (kgC m^{-2} month^{-1})				ET (mm month^{-1})			
	OBS (kgC m^{-2} month^{-1})	PV RMSE	Ground RMSE	AVIRIS RMSE	OBS (kgC m^{-2} month^{-1})	PV RMSE	Ground RMSE	AVIRIS RMSE	OBS (mm month^{-1})	PV RMSE	Ground RMSE	AVIRIS RMSE
SJER	0.045	0.032	0.026 (−19%)	0.026 (−19%)	−0.0002	0.059	0.022 (−63%)	0.021 (−64%)	27	19	19 (0%)	20 (+4%)
Soaproot	0.090	0.081	0.025 (−69%)	0.023 (−72%)	0.047	0.071	0.026 (−64%)	0.025 (−64%)	52	23	21 (−11%)	21 (−9%)
P301	0.085	0.059	0.028 (−51%)	0.034 (−42%)	0.064	0.060	0.028 (−54%)	0.033 (−46%)	52	32	24 (−26%)	24 (−23%)
Shorthair	0.040	0.11	0.019 (−83%)	0.021 (−82%)	0.021	0.078	0.026 (−67%)	0.024 (−69%)	33	42	29 (−31%)	34 (−19%)

Annual fluxes	GPP (kgC m^{-2} year^{-1})				NEP (kgC m^{-2} year^{-1})				ET (mm year^{-1})			
	OBS (kgC m^{-2} year^{-1})	PV RMSE	Ground RMSE	AVIRIS RMSE	OBS (kgC m^{-2} year^{-1})	PV RMSE	Ground RMSE	AVIRIS RMSE	OBS (mm year^{-1})	PV RMSE	Ground RMSE	AVIRIS RMSE
SJER	0.55	0.25	0.18 (−29%)	0.18 (−27%)	−0.0025	0.27	0.11 (−59%)	0.11 (−58%)	324	141	141 (0%)	140 (0%)
Soaproot	1.13	0.67	0.14 (−79%)	0.11 (−83%)	0.58	0.40	0.10 (−74%)	0.09 (−76%)	621	95	39 (−59%)	41 (−56%)
P301	1.02	0.35	0.19 (−46%)	0.26 (−24%)	0.77	0.41	0.25 (−39%)	0.32 (−23%)	625	182	104 (−41%)	111 (−38%)
Shorthair	0.48	1.10	0.07 (−94%)	0.12 (−89%)	0.25	0.66	0.05 (−93%)	0.12 (−82%)	401	333	150 (−55%)	211 (−37%)

Note: Values in parentheses are percentage reduction in RMSE when running the Ground-based and AVIRIS-initialized simulations compared to the PV-initialized simulations.

Abbreviations: AVIRIS, Airborne Visible/Infrared Imaging Spectrometer; ET, evapotranspiration; GPP, gross primary productivity; NPP, net ecosystem productivity; RMSE, root-mean squared error.

both the ground-based and AVIRIS-based initialized predictions still over-estimate ET in 2011 at SJER and Shorthair, and still under-estimate ET at Soaproot and P301 in 2012 and 2013.

The corresponding annual ET fluxes are shown in Figure 7e–h. The observed annual ET values were 324, 621, 625 and 401 mm H_2O year^{-1} at SJER, Soaproot, P301, and Shorthair, respectively (Figure 7e). The PV simulations (Figure 7f) predicted more uniform ET across the four sites—with higher mean ET at SJER and Shorthair, similar to lower mean ET at Soaproot and P301, respectively, and higher levels of inter-annual variability at all sites. RMSEs across the four sites were 141, 95, 182, 333 mm H_2O year^{-1} compared with observed fluxes. The ground-based and AVIRIS-based annual ET estimates showed no improvement at SJER, but more closely matched the observations at Soaproot, P301 and Shorthair with RMSEs of 141, 39, 104 and 150 mm H_2O year^{-1}, respectively, representing reductions of 0%, 59%, 41% and 55% in RMSEs at SJER, Soaproot, P301, and Shorthair (see Table 3). Similarly, the AVIRIS-based initializations predicted annual ET with RMSEs of 140, 41, 111, 211 mm H_2O year^{-1} representing 56%, 38% and 37% reductions in RMSE at Soaproot, P301 and Shorthair, respectively, over the PV-initialized simulations, but no reduction in RMSE at SJER (see Table 3).

3.2 | Regional-level analysis

3.2.1 | Carbon fluxes

The regional predictions of GPP and NEP during the 2010–2014 period are shown in Figure 8. Prior to the onset of the 2012 drought, rates of carbon uptake (GPP, left-hand panels) were lowest in the western, low-elevation portion of the simulation domain (<1000 m), moderate in the eastern, high-elevation region (>2200 m) and highest in the central, mid-elevation region (1000–2200 m). Following the onset of the drought in 2012, GPP decreased in all regions, with reductions of 18.5% at low elevations (0.161–0.131 kgC m^{-2} year^{-1}), 22% at high elevations (0.348–0.272 kgC m^{-2} year^{-1}) and the largest reduction at mid-elevations of 50% (0.733–0.369 kgC m^{-2} year^{-1}). Total GPP for the region decreased following the onset of the 2012 drought from around 310 ktC year^{-1} in 2010–2011 to 184 ktC year^{-1} in 2012–2014, a 40% decrease in GPP.

Rates of carbon storage predicted over the simulation domain (NEP, Figure 8 right-hand panels) show similar spatial patterns to GPP, and a similar pattern of decline following the 2012 drought: NEP is lowest at low-elevations (<1000 m), moderate in the eastern, high-elevation region (>2200 m) and highest in the central, mid-elevation region (1000–2200 m). Prior to the onset of the 2012 drought, areas below 1000 m elevation were weak sources of carbon (−0.041 kgC m^{-2} year^{-1}), mid-elevations were strong carbon sinks (0.377 kgC m^{-2} year^{-1}), and high elevations were moderate sinks of carbon (0.168 kgC m^{-2} year^{-1}). Following the onset of the drought in 2012, NEP decreased markedly in the mid-elevation region by 84% (0.377–0.059 kgC m^{-2} year^{-1}) and in the high-elevation region by 43% (0.168–0.096 kgC m^{-2} year^{-1}) but remained similar to pre-drought levels in the low elevation region (−0.041 to −0.040 kgC m^{-2} year^{-1}). The total carbon sequestered for the region fell by 83% from 94.11 and 144.19 ktC year^{-1} in 2010 and 2011, to 25.52, 17.53 and 10.63 ktC year^{-1} in 2012, 2013 and 2014, respectively (Figure 8 right-hand panels).

The elevational trends in regional GPP and NEP and the accompanying pattern of ecosystem composition derived from imaging spectrometry measurements are shown in Figure 9. Focusing initially on the relationships between ecosystem composition and carbon fluxes prior the onset of the drought (i.e. during 2010 and 2011), we observe that the ecosystems below 1000 m elevation are primarily comprised of Grass/Shrubs and Oaks/Western Hardwood PFTs. Within this elevation band, as elevation increases from 200 to 1000 m, the abundance of Oak/Western Hardwoods increases and non-vegetated land cover decreases (grey and red bars in Figure 9c) and both GPP (Figure 9a) and NEP (Figure 9b) increase as function of elevation: GPP increases from under 0.1 kgC m^{-2} year^{-1} at 200 m to around 0.4 kgC m^{-2} year^{-1} at 1000 m (Figure 9a), and NEP increases from around −0.2 kgC m^{-2} year^{-1} at 200 m to around 0.15 kgC m^{-2} year^{-1} at 1000 m (Figure 9b). Above 1000 m elevation, Fir–Cedars and Western Pine both increase in abundance and Grass/Shrub and non-vegetated cover continue to decline in abundance. Coincident with these changes in ecosystem composition, are rapid increases in the pre-drought levels of GPP and NEP as a function of elevation, with GPP increasing to around 0.85 kgC m^{-2} year^{-1}, and NEP increasing to above 0.4 kgC m^{-2} year^{-1} at 1200 m (Figure 9a,b). At mid-elevations between 1000 and 2200 m, ecosystems are comprised of a mixture of Fir/Cedar, Western Pines and Oaks/Western Hardwoods and, prior to the drought, these ecosystems had the highest associated rates of productivity and carbon storage, with GPP reaching between 0.6 and 1.0 kgC m^{-2} year^{-1} and NEP between 0.27 and 0.57 kgC m^{-2} year^{-1}. Above 2200 m, ecosystem composition shifts again, with declining abundances of Western Pines, Fir/Cedar PFT and increasing amounts of the High Pine PFT and non-vegetated cover as elevation increases. Associated with this compositional shift are declines in both productivity and carbon storage with GPP decreasing from around 0.4 kgC m^{-2} year^{-1} at 2200 m to under 0.2 kgC m^{-2} year^{-1} at 3000 m and NEP decreasing from around 0.2 kgC m^{-2} year^{-1} at 2200 m to near zero at 3000 m.

Following the onset of the drought, in low-elevation ecosystems (<1000 m), GPP and NEP are similar to their pre-drought levels at elevations between 200–500 m, but GPP decreases by around 0.05 kgC m^{-2} year^{-1} at 1000 m (Figure 9a), and NEP decreases by around 0.07 kgC m^{-2} year^{-1} at 1000 m (Figure 9b). Mid-elevation ecosystems between 1000 and 2200 m had the largest reductions in GPP and NEP following the onset of the drought, with GPP decreasing by around 0.3 to 0.5 kgC m^{-2} year^{-1} and NEP decreasing by around 0.25 to 0.45 kgC m^{-2} year^{-1} compared to their pre-drought fluxes. Furthermore, each successive year of drought resulted in lower GPP and NEP fluxes with 2014 being the lowest productivity

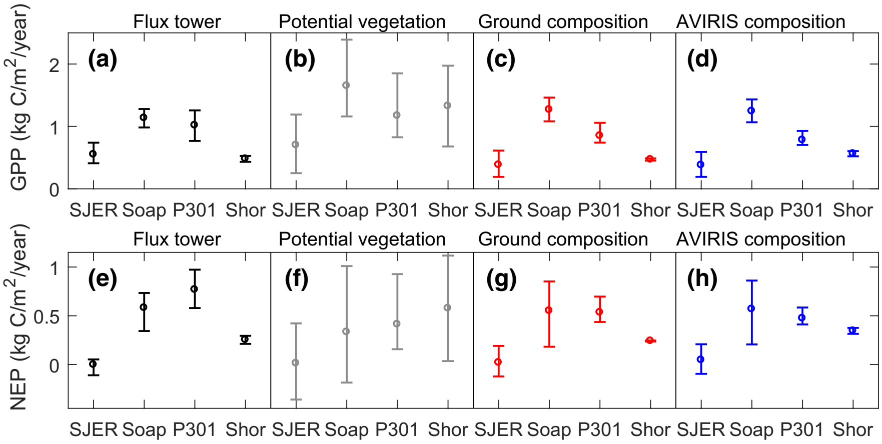

FIGURE 6 Average annual and inter-annual variability in GPP and NEP predictions obtained from potential vegetation simulations (b, f), from ground-based composition-initialized (c, g) and AVIRIS-based composition-initialized (d, h) simulations the ED2 model. These are compared with observed fluxes (a, e) from the four SSCZO flux tower sites over variable years; SJER (2010–2014), Soaproot (2011–2014), P301 (2009–2014) and Shorthair (2010–2011). AVIRIS, Airborne Visible/Infrared Imaging Spectrometer; GPP, gross primary productivity; NEP, net ecosystem productivity; Shor, Shorthair; SJER, San Joaquin Experimental Range; Soap, Soaproot; SSCZO, Southern Sierra Critical Zone Observatory

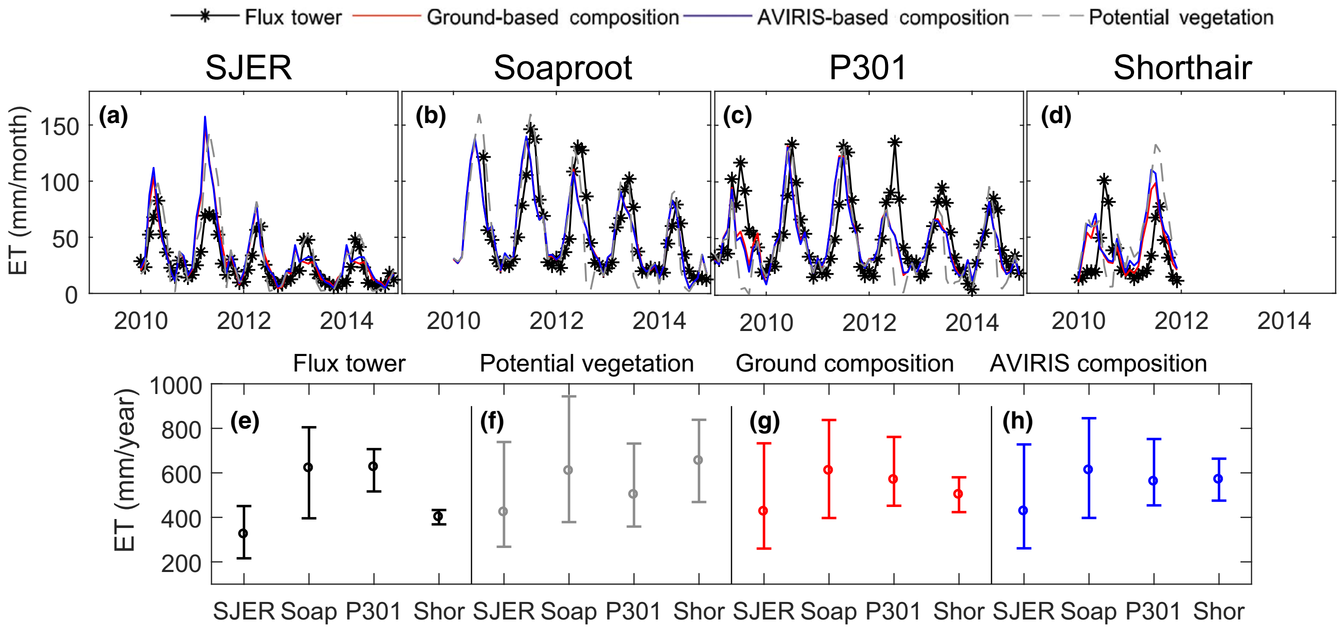

FIGURE 7 Predicted versus observed seasonal (a–d) and average annual and inter-annual (e–h) ET fluxes at the four flux tower evaluation sites; SJER, Soaproot, P301 and Shorthair. Black lines show the observed ET fluxes; remaining lines show the predictions of the ED2 terrestrial biosphere model when initialized with: ground-based estimates of canopy composition (red lines); AVIRIS-based estimates of canopy composition (blue lines) and canopy composition estimated from an equilibrium potential vegetation simulation (grey lines). The annual and inter-annual fluxes in (e–h) are over variable years; SJER (2010–2014), Soaproot (2011–2014), P301 (2009–2014) and Shorthair (2010–2011). AVIRIS, Airborne Visible/Infrared Imaging Spectrometer; ET, evapotranspiration; Shor, Shorthair; SJER, San Joaquin Experimental Range; Soap, Soaproot

year throughout much of the mid-elevation region. Above 2200 m, high-elevation ecosystems experienced moderate reductions in GPP and NEP, with both GPP and NEP decreasing by around 0.1 kgC m^{-2} $year^{-1}$ compared with pre-drought levels. Seasonally, the largest declines in NEP occurred in the summer months, where the mid-elevation ecosystems switched from being a sink of carbon to a source (see Figure S4).

3.2.2 | Water and energy fluxes

The regional patterns of transpiration and evaporation during the 2010–2014 period are shown in Figure 10. Prior to the drought, the average rate of canopy transpiration across the region in 2010–2011 was approximately 120 mm $year^{-1}$ (Figure 10a,b); however, the canopy transpiration exhibited marked spatial variation (Figure 10a,b),

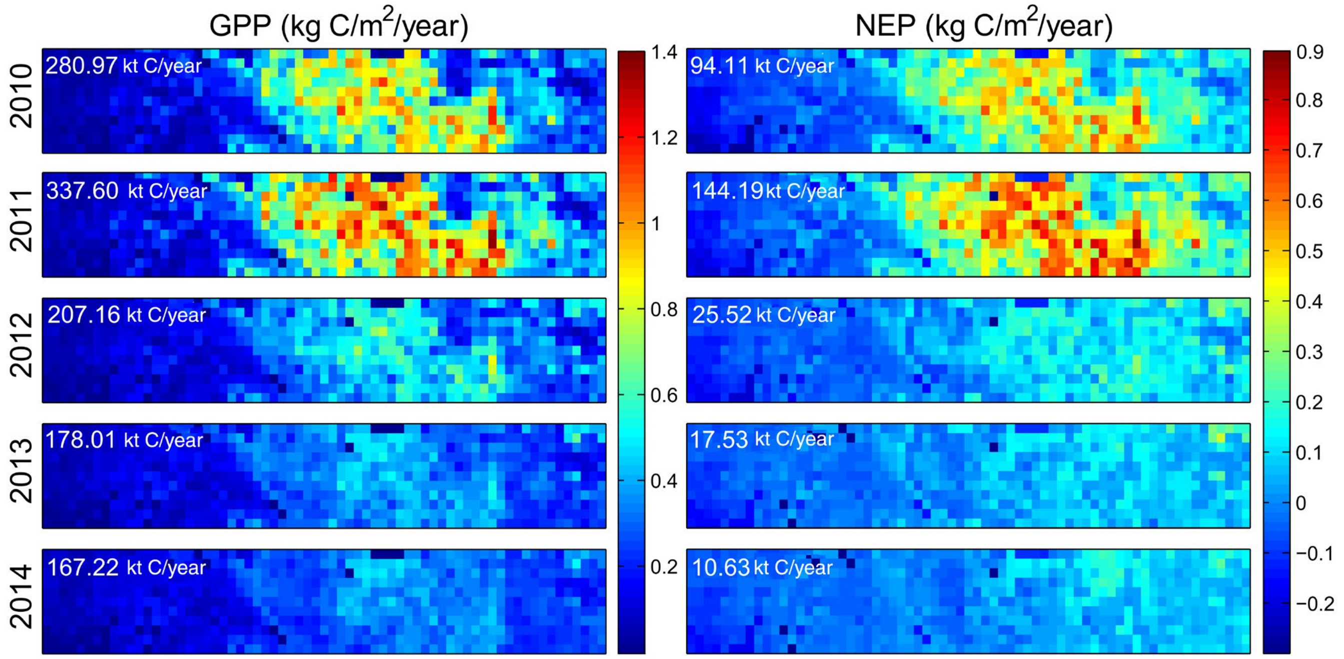

FIGURE 8 Annual spatial patterns and trends in regional gross primary productivity (GPP) and net ecosystem productivity (NEP) for the years 2010–2014. Total regional carbon fluxes per year are presented in the top left of each panel

which generally mirrors the patterns of GPP fluxes (Figure 8) with relatively high (average 214 mm year^{-1}) rates of transpiration in mid-elevation areas (1000–2200 m), moderate-to-low transpiration rates (average 104 mm year^{-1}) in high-elevation western regions (>2200 m) and low (average 39 mm year^{-1}) transpiration rates at low elevations (<1000 m).

As Figure 10 illustrates, following the onset of the drought, regional transpiration losses decreased by 33% from their pre-drought value of 120 mm year^{-1} to around 80 mm year^{-1}: the largest losses in canopy transpiration occurred in the mid-elevation (1000–2200 m) areas where transpiration decreased by 44%, from 214 mm year^{-1} in 2010–2011 to 119 mm year^{-1} in 2012–2014. In contrast, low- (<1000 m) and high-elevation (>2200 m) regions exhibited considerably smaller declines in canopy transpiration with declines of 3% and 9%, respectively (pre-drought transpiration rates of 38.9 and 104 mm year^{-1} declined to 37.7 and 95 mm year^{-1}, respectively). As shown in Figure S5, the large reductions in transpiration of the mid-elevation regions were caused by significant increases in stomatal closure.

Evaporation rates were considerably higher than transpiration, with an average pre-drought (2010–2011) evaporative water loss at around 640 mm year^{-1} (Figure 10c,d). Evaporation exhibits a more uniform pattern across space than transpiration (Figure 10c), with low- (<1000 m), mid- (1000–2200) and high-elevation (>2200) evaporation rates at 687, 629 and 553 mm year^{-1}, respectively. Following the onset of the drought (2012–2014), evaporative water loss across the region decreased by 53% from 640 to 303 mm year^{-1}. Low- to mid-elevation regions experienced higher evaporative losses than high elevations following the onset of the drought period, with 2012–2014 evaporation rates of 301, 297 and 319 mm year^{-1},

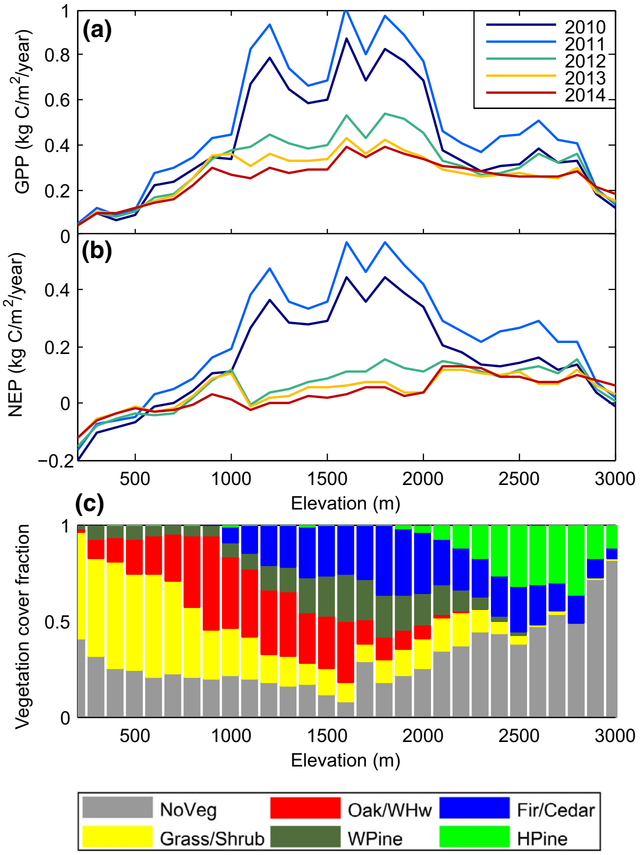

FIGURE 9 Annual trends in terrestrial carbon fluxes [(a) GPP and (b) NEP] across the elevational gradient. Elevation distributions of ecosystem composition derived from imaging spectrometry is shown in (c), as the fraction of vegetation cover occupied. GPP, gross primary productivity; NEP, gross primary productivity

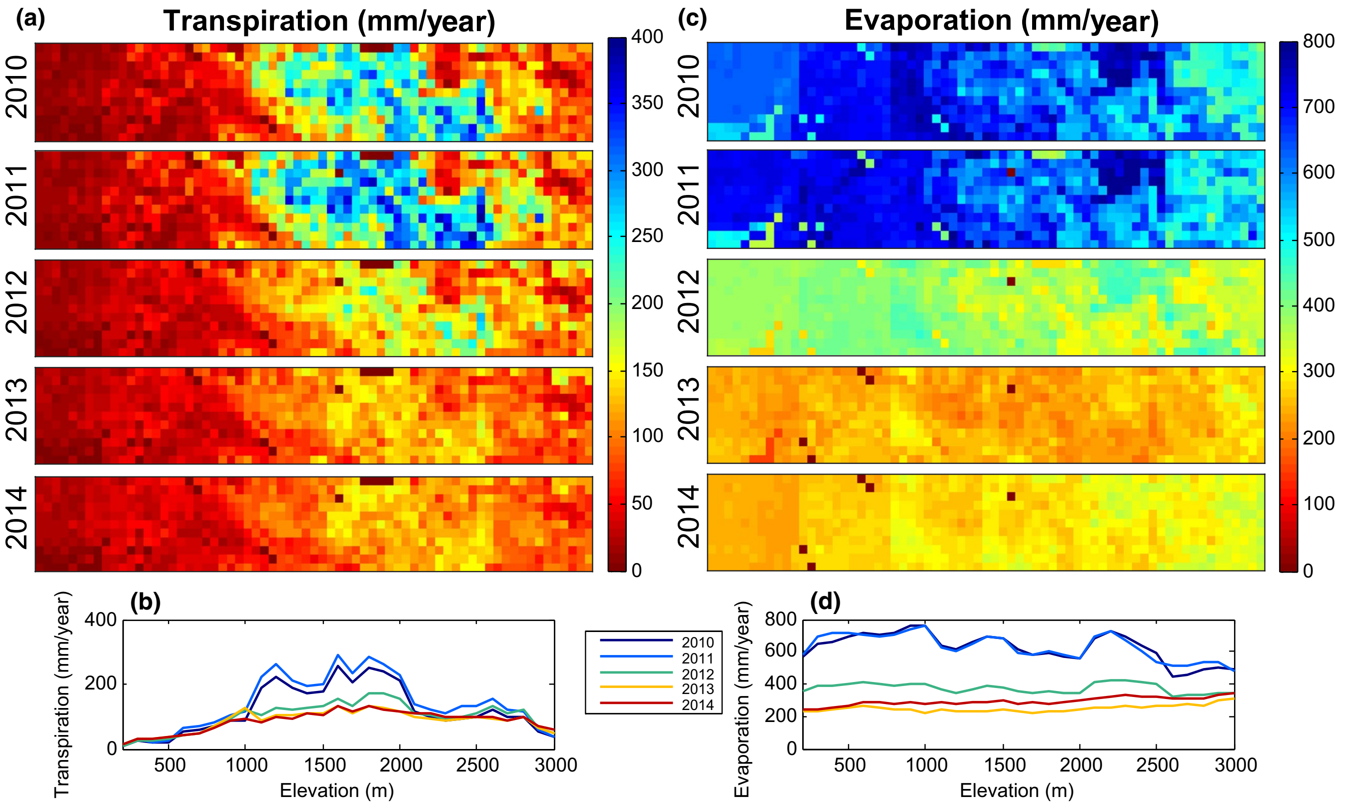

FIGURE 10 Annual spatial patterns and trends in transpiration (a, b) and evaporation (c, d) for years 2010–2014. Panels (b) and (d) show annual water fluxes across the elevational gradient. Banding, especially in (c), arises from edges in each grid cell of the NLDAS regional meteorology product. NLDAS, North American Land Data Assimilation

respectively (reductions of 56%, 53% and 42%). The associated changes in the pattern of sensible heat flux over the region are described in Appendix 2.

3.2.3 | Evaluation of the sources of error in the regional simulations

The impacts of the NLDAS regional meteorological forcing and the regional FIA-based estimate of forest structure on the model's predictions were assessed by comparing the predictions of the regional simulations against the prediction of simulations using observed meteorological forcing and observed canopy structure at the four flux-tower sites (Figure S6). As described in more detail in Appendix 2, this analysis indicates that the NLDAS regional meteorology is a more significant source of error in the regional simulations than inaccuracies in either the FIA-derived estimate of ecosystem structure or inaccuracies the AVIRIS-derived estimate of regional composition.

3.2.4 | Growth and mortality

Above-ground-biomass ecosystem growth and mortality spatial patterns for years 2010–2014 are shown in Figure 11. In 2010–2011, prior to the onset of the drought, average above-ground biomass (AGB) growth across the region was 0.10 kgC m^{-2} year^{-1} and rates of AGB growth at low-, mid- and high-elevation growth were 0.03, 0.18 and 0.10 kgC m^{-2} year^{-1}, respectively (Figure 11a,b). In 2012–2014, the average AGB growth decreased by 71% to 0.03 kgC m^{-2} year^{-1}. The most marked declines, both in absolute and relative terms, occurred at mid-elevations (1000–2200 m) where average accumulation decreased to 0.04 kgC m^{-2} year^{-1} (a 75% decrease). Low-elevation (>1000 m) and high-elevation (>2200 m) areas also declined significantly to 0.008 and 0.04 kgC m^{-2} year^{-1} (72% and 59% reductions, respectively). The most severe declines occurred in 2014, the final year of the drought in which AGB growth declined by 77%, 91% and 78% in low-, mid- and high-elevation regions, respectively, compared with their average pre-drought values.

With regard to AGB mortality, in 2010–2011, prior to the onset of the drought, average AGB mortality across the region was at 0.026 kgC m^{-2} year^{-1} (Figure 11c), with rates at low- (<1000 m), mid- (1000–2200 m) and high elevations (>2200 m) of 0.005, 0.038 and 0.050 kgC m^{-2} year^{-1}, respectively. Following the onset of the drought in 2012, average AGB mortality increased to 0.031 kgC m^{-2} year^{-1} in 2012, 0.083 kgC m^{-2} year^{-1} in 2013 and then to 0.24 kgC m^{-2} year^{-1} in 2014, reflecting mortality increases of 19%, 219% and 823%, respectively, over the average AGB mortality during the pre-drought period. Similar to growth, the most severe effects were in 2014; however, there was a notable lag in the temporal trend of mortality compared with growth: while significant declines in growth occurred

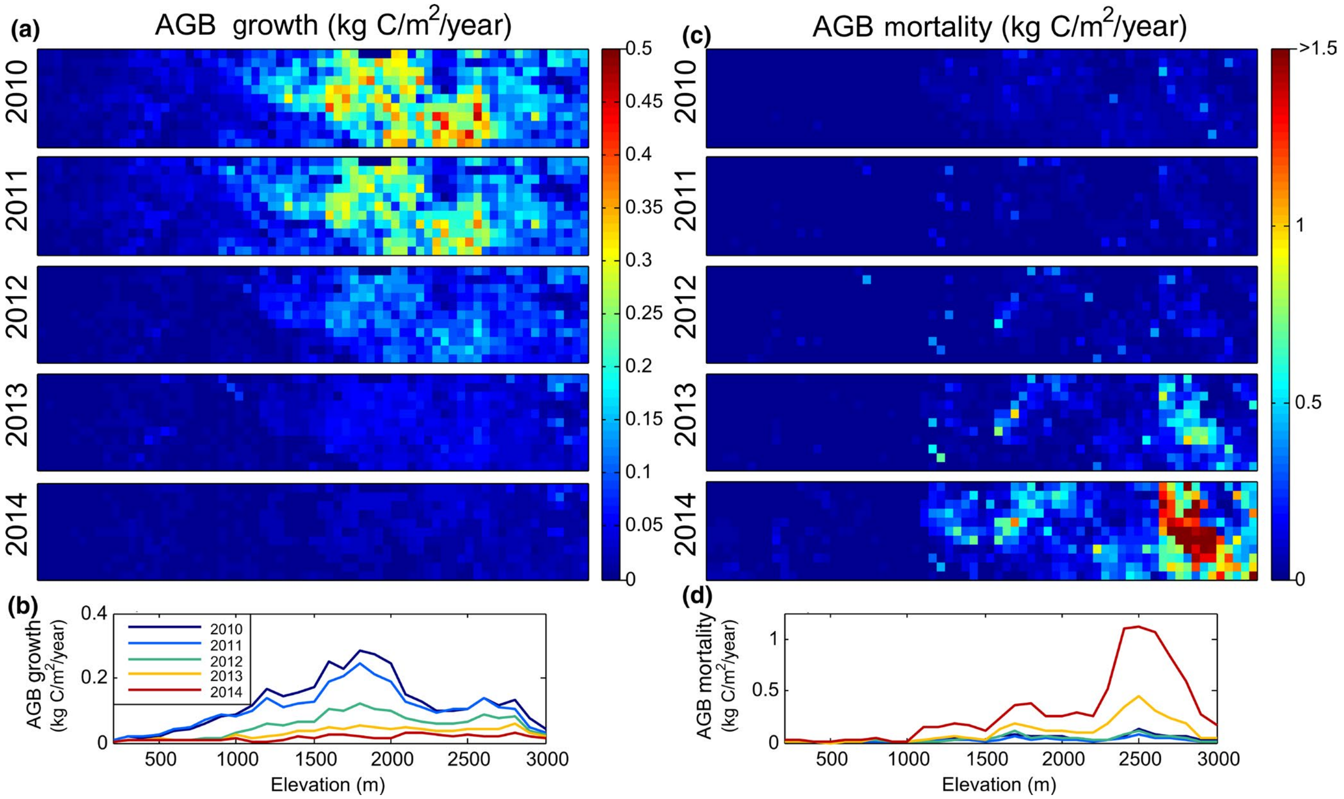

FIGURE 11 Spatial patterns and trends in above-ground biomass (AGB) growth (a, b) and mortality (c, d) for years 2010–2014. Panels (b) and (d) show the trends in annual AGB growth and mortality across the elevational gradient

in 2012 (Figure 11a), significant increases in mortality did not occur until 2013 and 2014 (Figure 11c).

Similar to AGB growth, the highest increases in mortality rates occurred in mid- and high-elevation areas with increases in 2012, 2013 and 2014 to 0.043, 0.090 and 0.24 kgC m^{-2} $year^{-1}$ for mid-elevations and to 0.055, 0.24 and 0.75 kgC m^{-2} $year^{-1}$ for high elevations, receptions. This reflects mortality rates in 2014 of 6 and 15 times higher than the average AGB mortality in the mid- and high elevation, respectively, during the pre-drought period. Lower elevation areas also increased in mortality in 2012, 2013 and 2014, but to a lesser extent −0.009, 0.008 and 0.016 kgC m^{-2} $year^{-1}$, respectively. The regional patterns of AGB growth and mortality for the different PFTs are shown in Figure S7. As can be seen in this supplementary figure, the high mortality rates in 2013–2014 for mid-to-high-elevation regions (Figure 11c,d) correspond mostly to losses of Fir/Cedar and High Pine (Figure S7g,h).

3.2.5 | Effects of ecosystem composition and structure on the magnitude of drought impacts

Figure 12 shows how the magnitude of the drought impacts on carbon, water and biomass dynamics vary as a function of forest composition and structure. The *y*-axis of each panel shows the difference in the value of a given quantity in 2014 compared with the pre-drought years, the *x*-axis shows the pre-drought basal area per grid-cell, and the colours of each point reflect the dominant woody PFT within each simulation grid cell. As the figure illustrates, drought-induced decreases in AGB growth, NEP, GPP and transpiration are significantly correlated with pre-drought forest basal area ($R^2 = 0.69$, 0.63, 0.56 and 0.52, respectively; see Figure 12d,a,b,e, and Table 4). A similar, but less strong, pattern is seen in drought-induced increases in AGB mortality and declines in evaporation (R^2 = 0.42 and 0.38, respectively; see Figure 12c,f; Table 4).

As the colours in Figure 12 illustrate, the magnitudes of the drought impacts are also significantly affected by ecosystem composition. At low basal areas (<10 m^2 ha^{-1}), the largest drought-induced declines in GPP, NEP, transpiration, and AGB growth occurred in Oak/Western Hardwood- and Western Pine–dominated areas, while the declines in Fir/Cedar- and High Pine-dominated areas were lower. At moderate and high basal areas (>10 m^2 ha^{-1}), the magnitudes of declines GPP, NPP, transpiration, and AGB growth in Fir/Cedar-dominated areas generally increased to levels similar to, or higher than, Oak/Western Hardwood- and Western Pine-dominated areas with a similar basal area, whereas rates of decline in High Pine-dominated areas remain relatively low by comparison (Figure 12a,b,d,e). The effects of composition on AGB mortality (Figure 12c) exhibit a different pattern: for a given basal area, rates of AGB mortality tended to be higher in High Pine-dominated and some Fir/Cedar-dominated areas compared with Oak-Western Hardwood and Western Pine-dominated areas (Figure 12c).

The results of associated regression models are shown in Table 4. In univariate models Fir/Cedar abundance is the best single predictor

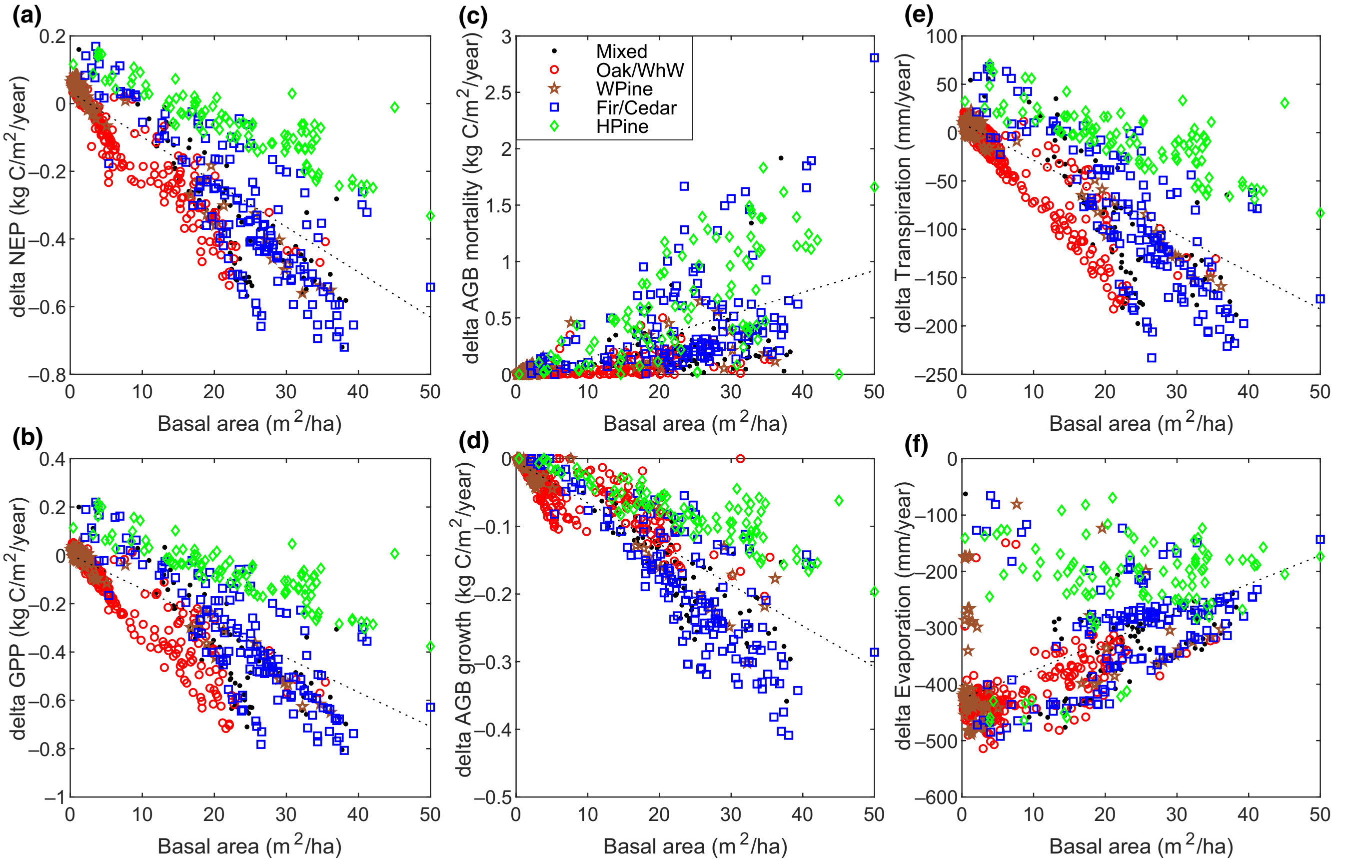

FIGURE 12 Relationships between forest composition and structure and the impacts of the 2012–2015 California drought and six metrics of ecosystem performance in the regional ED2 simulations: (a) net ecosystem productivity, (b) gross primary productivity, (c) AGB mortality, (d) AGB growth, (e) transpiration, (f) evaporation. Points reflect the changes (Δ) in the given ecosystem performance metric between 2014 and their pre-drought averages across the 1 km grid-cells of the simulation region shown in Figures 8, 10 and 11. Forest composition categories reflect dominant woody PFTs and include a mixed PFT category. AGB, above-ground biomass; GPP, gross primary productivity; NEP, gross primary productivity; PFT, plant functional type

of drought-induced decreases in NEP (R^2 = 0.66), GPP (R^2 = 0.56), AGB growth (R^2 = 0.803), and transpiration (R^2 = 0.56). High Pine abundance is the best single predictor of drought-induced increases in AGB mortality (R^2 = 0.474), whereas basal area is the best single predictor of changes in evaporation (R^2 = 0.38). Combined measures of ecosystem structure and composition explained most of the between grid-cell variability in drought-induced declines of NEP, GPP, AGB growth, and transpiration (R^2 values of 0.94, 0.91, 0.91 and 0.89, respectively); and to a lesser degree variation in AGB mortality and evaporation increases (R^2 of 0.63 and 0.58, respectively). Elevation (not shown) was a weak predictor of drought-induced declines in NEP, GPP, AGB growth, and transpiration (R^2 = 0.045–0.2) but was a reasonable predictor of drought-induced increases in AGB mortality and declines in evaporation (R^2 = 0.39 and 0.50, respectively).

4 | DISCUSSION

This study has shown how spatially resolved estimates of regional PFT composition derived from imaging spectrometry measurements can provide important constraints on terrestrial biosphere model predictions of regional-scale carbon, water and energy fluxes and accompanying AGB dynamics.

4.1 | Evaluation of the imaging spectrometry-constrained model

Incorporating the imaging spectrometry-derived estimates of above-ground canopy composition into the ED2 terrestrial biosphere model substantially improved the model's predictions of gross (GPP) and net (NEP) carbon fluxes at the four flux-tower sites (Figures 5 and 6). Monthly and annual GPP RMSEs were reduced by 19%–89% and monthly and annual NEP RMSEs by 23%–82% compared with the PV-initialized simulations (Table 3), and the magnitude of the improvements are similar to those achieved when the model was initialized with ground inventory estimates of canopy composition. The carbon flux predictions of the imaging spectrometry-initialized simulations were most similar to the ground inventory-initialized simulations at SJER and Soaproot reflecting the high-level of accuracy of the imaging spectrometry composition estimates at these two sites (Figure 2).

TABLE 4 Single and multivariate regressions between imaging spectroscopy-derived ecosystem composition and FIA-based structure predictor variables, and predicted drought impacts on key carbon, biomass and water flux metrics

Drought impact (response variable)	Regression model	Basal area (m^2 ha^{-1})	Grass shrub (fraction)	Oak WhW (fraction)	WPine (fraction)	Fir Cedar (fraction)	HPine (fraction)	Intercept	R^2	RMSE
Δ NEP (kgC m^{-2} $year^{-1}$)	Basal area only	−0.01	-	-	-	-	-	0.04	0.63	0.12
	Single best predictor	-	-	-	-	−1.02	-	−0.007	0.66	0.12
	Multivariate	−0.01	−0.07	−0.32	−0.22	−0.37	0.50	0.14	0.94	0.05
Δ GPP (kgC m^{-2} $year^{-1}$)	Basal area only	−0.01	-	-	-	-	-	0.003	0.56	0.15
	Single best predictor	-	-	-	-	−1.07	-	−0.04	0.56	0.15
	Multivariate	−0.02	−0.13	−0.39	-	−0.29	0.80	0.14	0.91	0.07
Δ AGB mortality (kgC m^{-2} $year^{-1}$)	Basal area only	0.02	-	-	-	-	-	−0.05	0.42	0.23
	Single best predictor	-	-	-	-	-	2.02	0.10	0.47	0.26
	Multivariate	0.01	-	−0.31	−0.46	0.39	1.11	0.05	0.63	0.22
Δ AGB growth (kgC m^{-2} $year^{-1}$)	Basal area only	−0.01	-	-	-	-	-	−0.005	0.69	0.05
	Single best predictor	-	-	-	-	−0.49	-	−0.02	0.80	0.04
	Multivariate	−0.004	−0.01	-	−0.15	−0.24	0.16	0.01	0.91	0.03
Δ transpiration (mm $year^{-1}$)	Basal area only	−3.85	-	-	-	-	-	9.84	0.52	44.82
	Single best predictor	-	-	-	-	−301.28	-	−1.36	0.56	42.76
	Multivariate	−4.89	−40.99	−83.73	-	−87.72	256.95	45.62	0.89	21.34
Δ evaporation (mm $year^{-1}$)	Basal area only	5.09	-	-	-	-	-	−425.90	0.38	78.42
	Single best predictor	5.09	-	-	-	-	-	−425.90	0.38	78.42
	Multivariate	6.68	−143.64	−267.04	−268.11	−217.11	−159.89	−300.51	0.60	63.62

Note: The six response variables reflect changes between 2014 and their pre-drought averages. The relationships reflect single regressions using structure (basal area) only, single regressions with the best predictor, and multivariate regressions.

Abbreviations: AGB, above ground-biomass; FIA, forest inventory and analysis; GPP, gross primary productivity; NPP, net ecosystem productivity; RMSE, root-mean squared error.

However, at P301 and Shorthair, the differences between the imaging spectrometry-initialized and ground inventory-initialized carbon flux estimates were larger because of over-estimation of the abundance of the High Pine PFT at P301, and under-estimation of its abundance at Shorthair (Figure 2). The lower accuracy of the PFT composition estimates at these two sites arises because of the poorer spectral separability of the High Pine and Fir/Cedar PFTs: Fir-Cedar and High Pine end-member spectra were only sufficiently distinct in 47% and 55% of wavelengths during the fall and spring (Bogan et al., 2019).

The improvements in the accuracy of carbon flux predictions obtained in the imaging spectrometry-constrained simulations (yearly NEP RMSE reductions of 23%–82% and GPP reductions of 24%–89%) are comparable with those obtained in a previous analysis (Antonarakis et al., 2014), which used imaging-spectrometry measurements to constrain terrestrial biosphere model predictions of carbon fluxes in a temperate forest ecosystem in the North-eastern United States (36%–49% reductions in NEP RMSEs, and 53%–121% reductions in GPP RMSEs). This analysis builds upon Antonarakis et al. (2014) by expanding the evaluation of how imaging spectrometry-derived estimates of ecosystem composition affect predictions of ecosystem function to encompass water fluxes as well as carbon fluxes. At Soaproot, P301 and Shorthair, incorporating imaging spectrometry-derived estimates of ecosystem composition reduced the monthly and annual RMSEs of ET at these sites by 9%–56% compared with the PV-initialized simulations (Table 3). As with GPP and NEP, the magnitudes of these improvements in ET were comparable with the improvements obtained with ground-inventory initialized simulations at the three sites, which ranged from 11% to 59%. However, the impacts of imaging-spectrometry initialization on monthly or annual water fluxes at SJER were minimal. These were similar to the effects of the ground-inventory initialization on the accuracy of water flux predictions at SJER, which saw no change in monthly or annual fluxes (Table 3). These remaining mismatches between the model and observations at SJER, as well as seasonal overestimations at SJER and Shorthair and under-estimation during drought years at P301, reflect underlying deficiencies in the model's formulation rather than errors arising from incorrect specification of the composition of the plant canopy.

4.2 | Impacts of the 2012–2015 California drought on regional carbon, water and energy fluxes

In second part of this study, the imaging spectrometry-constrained model was used to predict regional carbon, water and energy fluxes over a 737 km^2 area spanning a large elevation gradient in the Sierra Nevada Mountain range over a 5-year period spanning the 2012–2015 Californian drought (Figures 8–12). As noted in the Introduction, this drought was a one-in-thousand-year event (Robeson, 2015), which left the state with an average rain deficit of around 500 mm, equal to a year's rainfall (Cole & Gray, 2015).

Although there have been several empirical assessments of the impacts of the 2012–2015 drought (Asner et al., 2016; Byer & Jin, 2017; Goulden & Bales, 2019; Potter, 2016; Young et al., 2017), the results of this study provide new mechanistic insights and inference regarding the patterns and magnitudes of the drought's impacts on regional-scale carbon, water and energy fluxes across the diverse vegetation communities found across the region. Prior to the onset of drought in 2012, net carbon uptake (NEP) in the region was approximately 160 tC ha^{-1} year^{-1} resulting in a total uptake rate of 120 ktC year^{-1} across the region with the highest rates of uptake occurring in the functionally diverse, high basal area mid-elevation (1000–2200 m) forests (Figures 8 and 9). Following the onset of the drought in 2012, the region's carbon uptake declined markedly with the largest declines occurring in the mid-elevation forests which experienced a 50% decline in GPP and an 84% decrease in their NEP between 2012 and 2014 (Figures 8 and 9). This spatial pattern of drought impact on the region's carbon fluxes are consistent with Young et al.'s (2017) analysis of United States Forest Service aircraft photo survey measurements collected between 2009 and 2015, which found that trees in the drier, denser (higher basal area) forests of the Southern Sierra Nevada were more vulnerable to extreme drought. They suggested that this likely reflected the high demand and competition for water in these regions.

The predicted rapid and widespread declines in GPP and NEP following the onset of the drought in 2012 compared with the pre-drought years seen in Figures 8 and 9 is, as far as we are aware, a previously undocumented consequence the 2012–2015 drought. Comparison of the predicted and observed temporal patterns of GPP and NEP declines at the SJER, Soaproot and P301 flux tower sites provide some support for this conclusion. There are signs of reduced carbon uptake in 2012 in the observations at SJER and P301 (Figure 5, see also Goulden & Bales, 2019). However, at Soaproot, declines in GPP and NEP are not evident in either the observations or in the model predictions (Figure 5c,d), suggesting that the lack of response observed at this site was not indicative of what was occurring more broadly in the mid-elevation ecosystems during this period.

Alongside the marked declines in mid-elevation carbon uptake during 2012–2014 were marked declines in water fluxes (Figure 10) and associated shifts in the surface energy balance of the land surface (Figure S8). These findings are consistent with the results of a recent study by Goulden and Bales (2019) who analysed the impacts of the 2012–2015 drought by developing a statistical relationship between estimates of ET across a series of flux towers and NDVI and then using this ET–NDVI relationship to estimate impacts of the drought on regional water balance (cumulative precipitation minus ET). In particular, consistent with the results of Goulden and Bales (2019), our analysis indicates large-scale declines in ecosystem water balance in areas between 1000 and 2000 m elevation occurred during the drought period (Figure 10). Our resulting water fluxes and regional patters prior to the drought are also consistent with the literature (Goulden et al., 2012; Goulden & Bales, 2014), where transpiration in 2010–2011 (Figure 10) increased up to around 2000 m, with decreases at higher elevations attributed to cold limitation in California's upper Sierra Nevada ecosystems dominated by High Pines (Goulden & Bales, 2014).

Examination of the timing of the declines in ET in response to the drought seen at the flux-tower sites indicates that at the mid-elevation Soaproot and P301 sites the model predicted an earlier onset of declines in ET compared with the observations (summer 2012 vs. summer 2013; see Figure 7b,c; see also Goulden & Bales, 2019). One explanation for this discrepancy is that the plants have access to a significantly larger store of moisture than the SSURGO soil depth to bedrock survey data imply: soil analyses at Soaproot and P301 have revealed the presence of a significant weathered bedrock beneath the maximum 2 m of soil depth measured by SSURGO soil survey (O'Geen et al., 2018). The overall depth of the regolith varies spatially, but calculations taking this additional depth into account markedly increases (more than doubles) the amount of plant available water at sites between 600 and 2000 m (O'Geen et al., 2018). The presence of such deep moisture likely acts as significant additional moisture buffer that prolonged the onset of the drought's impact in regions where it was present. In addition, a previous analysis in temperate forest ecosystem indicates that the terrestrial biosphere model's partitioning of ET between evaporation and transpiration is biased significantly toward evaporation (Wehr et al., 2017), which may result in excessive water loss from the soil column and more rapid declines in canopy transpiration compared with the observations.

An earlier analysis of high-resolution airborne imaging spectrometry and multi-spectral satellite measurements (Asner et al., 2016) estimated that 80% of Californian forests experienced significant losses in canopy water content during the drought, with over 7% of forests experiencing canopy water loss greater than 30% (Asner et al., 2016). However, the results of this analysis imply that the effects of the drought are even larger when assessed in terms of its impact on the region's water and energy fluxes: regional transpiration and evaporation declined by 33% and 53%, respectively, compared with the pre-drought 2010–2011 period (Figure 10) with 43% of the region experiencing canopy water losses greater than 30%. Associated with these declines in evaporation and transpiration were increased levels of stomata closure (Figure S5) and a 51% increase in the sensible heat fluxes (Figure S8).

4.3 | Impacts of the 2012–2015 California drought on regional biomass dynamics

Rates of tree mortality increased substantially during the drought period: average canopy biomass mortality (trees greater than 20 cm diameter at breast height) was nine times higher in 2014 compared with levels during pre-drought years (Figure 11). This translates to over 400,000 trees in 2014, or an average per capita mortality rate of 535 trees km^{-2} $year^{-1}$, values that are nearly an order of magnitude higher than the pre-drought mortality levels (40,000 trees $year^{-1}$ or a per capita mortality rate of 55 trees km^{-2} $year^{-1}$, Figure S9). These estimates are broadly consistent with a USFS study (Young et al., 2017) that estimated that mortality in the Sierra Nevada increased by an order of magnitude from 10 to 25 trees km^{-2} $year^{-1}$ prior to the drought to 400–1000 trees km^{-2} in 2015.

Interestingly, in the regional simulations the declines in NEP and AGB biomass growth during 2012 presage the subsequent increases in mortality (Figures 8 and 11 respectively). This finding is consistent with the findings of empirical studies that have documented drought-induced declines in tree growth rates prior to the onset of drought-induced mortality (Berdanier & Clark, 2016; Ogle et al., 2000), and the finding of a remote sensing study of the recent California drought that found drought-induced declines satellite-derived vegetation indices in the year proceeding the onset of widespread forest mortality (Potter, 2016). From a regional ecosystem monitoring perspective, the early onset of drought-induced declines in above-ground productivity and biomass growth that occur in the model simulations implies that terrestrial biosphere models can also be used to identify areas that are vulnerable to large-scale die-offs if a drought event continues. This approach has two advantages over remote-sensing imagery-based analyses. First, widespread increases in mortality occurred 2 years after the onset of declines in growth, implying an improved ability to forecast mortality events compared with analyses of satellite-derived vegetation indices. Second, in contrast to remote sensing-based analyses (and also tree-core studies), the process-based nature of the terrestrial biosphere model used here enables forecasting of future changes in tree morbidity and mortality rates under a variety of future climate, atmospheric CO_2 concentration and forest management scenarios, and thus be used for contingency and scenario planning activities.

The spatial pattern of drought-induced mortality (Figure 11d) predicts that mortality losses are largest at high elevations (above 2500 m) with a secondary mortality peak around 1700 m. In an analysis of tree mortality in Sequoia National Park (approximately 140 km south of our study region), Paz-Kagan et al. (2017) found mortality in forest inventory plots distributed along a 1000–3000 m elevation gradient had peaks at 1600–1800 m and a secondary peak at 2400–2500 m. Although the model simulations conducted here predict that the high-elevation mortality peak was larger than the mid-elevation peak, the model's predictions of mortality peaks at 1700 and 2400 m accords with the spatial patterns found in the Paz-Kagan et al. (2017) study.

The pattern of mortality in the aerial surveys of Young et al. (2017) (Figure S9) also suggest high levels of mortality at mid-elevations. There are a several potential explanations for the more muted mid-elevation mortality peak in the model predictions: (i) the magnitude of the drought at mid-elevations may have been under-estimated due to inaccuracies in the meteorological forcing used to drive the model simulations; (ii) the degree of drought-tolerance in the Western Pine and Fir/Cedar PFTs may have been over-estimated due inaccuracies in the parameterization of their physiological and morphological attributes and (iii) the absence of insect-induced mortality in the biosphere model formulation. With regard to this latter point, several earlier studies noted that the mid- and high-elevation regions suffered high degrees of mortality through a combination of water stress and insect activity (USFS, 2015; Young et al., 2017), where according to Restaino et al. (2019), insect mortality was more dominant in mid-elevation Western Pine species (e.g. *P. Ponderosa* and *P. lambertiana*) compared with Fir/Cedar species (*A. concolor*, *C. decurrens*).

The mortality rates over the region during the drought period reflect the combined effects of the baseline level mortality plus the drought-induced mortality and insect-induced mortality. The ED2 terrestrial biosphere model does not include insect-induced mortality;

however, the model's mortality rate can be separated into a baseline and drought-induced mortality components (Figure S10, black bars and grey bars, respectively). Estimates of the combined impact of drought-induced and insect-induced mortality (Figure S10, white bars) arise from the difference in baseline (pre-drought years) and 2015 USGS aerial survey estimates of average mortality levels within hand delineated polygons. As the figure illustrates, over the mid-elevation regions (1000–2200 m), where Western Pines and Fir/Cedars dominate, combined drought- and insect-induced mortality was estimated by the USGS to be around four times larger than ED2 predicted drought-induced mortality (Figure S10). In contrast, the model's mortality rates at high elevations (>2200 m) exceed the USGS-derived combined drought-induced and insect-induced mortality rate estimate, suggesting that the model is over-estimating drought-induced mortality in these areas. This over-estimation may reflect inaccuracies in the meteorological forcing at high elevations; however, more likely it reflects inaccuracies in the underlying physiological and morphological parameterization of High Pine PFT in the ED2 model arising from the short observational time-series available to evaluate the model's carbon flux predictions at the Shorthair flux tower site.

4.4 | Influences of ecosystem composition and structure on drought impacts

The impacts of the drought on the ecosystems of the Sierra Nevada Mountain study region were largest over the functionally diverse, high basal area mid-elevation areas, where there were marked reductions in carbon (Figures 8 and 9), water (Figure 10a) and AGB growth (Figure 11a). As noted earlier, this is consistent with Young et al.'s (2017) assessment of the Californian drought over the Southern Sierra Nevada mountains, which found that drier, denser forests were more vulnerable to extreme drought, due to increased competition for water (Young et al., 2017) resulting in an increased risk of cavitation and/or depletion of carbon reserves (see McDowell et al., 2008). As seen in Figure 12 and Table 4, forest structure (here specified from regional FIA measurements) was a strong predictor of drought-induced increases in AGB mortality, and decreases in NEP, GPP, transpiration and AGB growth and was a moderate predictor of drought-induced decreases in evaporation. In addition, although we found that elevation was generally a poor predictor of the drought's impact on ecosystem performance, it was correlated with the magnitude of mortality increases, a finding that is consistent with the findings of Restaino et al.'s (2019) analysis.

However, as Figure 12 also illustrates, the strength of drought impacts is also significantly affected by canopy composition. For example. Oak/Western Hardwood and Western Pine dominated areas are associated with large drought-induced decreases in carbon and water fluxes (Figure 12a,b,e), but with lower increases in AGB mortality (Figure 12c), whereas Fir/Cedar-dominated areas are associated with large drought-induced decreases in carbon and water fluxes, combined with large decreases in drought-induced AGB growth and increases in AGB mortality, indicating more susceptibility to drought. Ecosystem composition is a marginally stronger single predictor than ecosystem structure for the impacts of the drought on carbon fluxes, transpiration, and AGB growth and mortality (Table 4), a finding that accords with the results of Paz-Kagan et al. (2017), who found significant species-specific variation in the impacts of the drought across the Sierra Nevada elevation gradient.

Finally, as the results of the multivariate regressions illustrate (Table 4), the effects of structure and composition are largely additive, and when combined, account for approximately 90% of the observed variation in drought impacts across the region. More generally, these findings provide impetus to refining and improving estimates of regional ecosystem composition and structure for use in both empirical and terrestrial biosphere model-based analyses such as this study. Studies of this kind could be used to identify locations which, due to their canopy composition and/or canopy structure, are likely to be particularly vulnerable to the impacts of droughts and other forms of climate extremes.

4.5 | Implications and future work

This study shows how terrestrial biosphere models can use imaging spectrometry derived estimates of current ecosystem composition to improve regional-scale predictions of carbon, water, and energy fluxes, and ecosystem dynamics. Accurate information on current ecosystem composition is critical for improving predictions of how terrestrial ecosystems are responding to climate variability and change. Traditional approaches, in which terrestrial biosphere simulations are initialized with output from a long-term equilibrium PV simulation, are problematic due to errors in climate forcing, the lack of adequate climate data and a lack of spatially resolved land-use and disturbance history information. For example, in the region analysed here, the history of fire disturbance, fire suppression and insect-induced mortality events are important drivers of differences in composition at the different elevations of the Sierra Nevada range (McKelvey et al., 1996; Schwartz et al., 2015; Taylor et al., 2016).

This study moves beyond approaches to specifying terrestrial ecosystem composition from global land cover products (e.g. Jung et al., 2007; Quaife et al., 2008) by (i) directly deriving regional PFTs from imaging spectrometry rather than linking land surface models with generic global land cover products; (ii) by differentiating appropriate PFTs ranging from woody to non-woody plant types and (iii) by representing sub-pixel scale heterogeneity in ecosystem canopy composition through exploiting the imaging spectrometer's high spectral resolution capabilities. An interesting avenue for future research on the effects of composition on ecosystem responses to drought is determining the key traits or trait combinations that underpin the differing responses of the PFTs across the domain.

This study also moves beyond the earlier imaging spectrometry-constrained terrestrial biosphere simulations of Antonarakis et al. (2014) in Four important ways. First, while Antonarakis et al. (2014) developed imaging spectrometry-constrained predictions for

~4 km^2 area within a single temperate forest biome, in this study, we developed imaging-spectrometry constrained predictions over a 740 km^2 region spanning a broad range of biome types, ranging from tree-grass savannahs to high-elevation conifer forests (Figure 4). This demonstrates the relevance of imaging spectrometry measurements for improving regional, and potentially global-scale, predictions of terrestrial ecosystem function. Second, in contrast to Antonarakis et al. (2014), that evaluated and analysed seasonal carbon flux predictions, this study evaluated and analysed a broader array of metrics of ecosystem function, including seasonal to interannual predictions of carbon, water and energy fluxes, and accompanying predictions of regional above-ground growth and mortality dynamics. Third, the analysis spanned a period of severe, region-wide drought, highlighting the relevance of imaging-spectrometry constrained terrestrial biosphere model simulations to calls for large-scale monitoring and forecasting of how ecosystems are impacted by climate variability and change (Clark et al., 2001; Dietze, 2017). Specifically, the findings of this study show the Californian drought of 2012–2015 impacted the Southern Sierra forests by decreasing NEP and GPP by 85% and 40% (Figures 8 and 9), decreased evaporation and transpiration by 53% and 33% (Figure 10), increasing sensible heat by 51% (Figure S8), decreasing growth by 71.5% (Figure 11a,b) and increasing mortality by 350% (Figure 11c,d).

Fourth, in contrast to the estimates of canopy composition used by Antonarakis et al. (2014) that were derived from high-resolution (6 m) imaging spectrometry measurements, the estimates of fractional PFT-composition used in this analysis were derived from 18-m resolution imaging spectrometry measurements (Bogan et al., 2019). The ability to constrain and improve terrestrial biosphere model predictions with coarser resolution imaging spectrometry measurements as demonstrated in this study implies that upcoming global, satellite-based imaging spectrometry missions, such as NASA's Surface Biology and Geology (SBG) mission (Cawse-Nicholson et al., 2021; NASEM, 2018), Germany's Environmental Mapping and Analysis Program (EnMAP) (Guanter et al., 2015) and Japan's Hyper-spectral Imager SUIte (HISUI) (Matsunaga et al., 2017), can substantially improve regional, continental and global-scale predictions of terrestrial ecosystem function.

In addition to spatially-resolved information on ecosystem composition, accurate spatially-resolved information on ecosystem structure is also critical for improving regional and global-scale predictions of how terrestrial ecosystems are responding to climate variability and change. In this analysis, information on canopy structure came from ground-based forest inventory measurements; however, future investigations will be able to combine imaging spectrometry measurements with remote sensing-based estimates of forest structure, such as those from the GEDI (Global Ecosystem Dynamics Investigation) waveform lidar (Dubayah et al., 2014, 2020; Hancock et al., 2019), or from planned radar instruments, such as the NASA-ISRO Synthetic Aperture Radar (NISAR) (Rosen et al., 2015) and the European Space Agency's BIOMASS (P-band POLinSAR) mission (Le Toan et al., 2011), and the instrument(s) for NASA's high-resolution global Surface Topography and Vegetation (STV) Targeted Observable (NASEM, 2018). A methodology for assimilating waveform lidar measurements of canopy structure into terrestrial biosphere models has already been established (Antonarakis et al., 2014). In the case of radar, there is potential to use radar's interferometric capability, to determine canopy height profiles similar to those estimated by lidar (e.g. Treuhaft et al., 2009), Alternatively, radar-derived biomass could also be used to adjust or correct the distribution of biomass derived from the spatially-extrapolated FIA plots in this study (i.e. Figure 4), as in Antonarakis et al. (2011).

Finally, in this study imaging spectrometry measurements were used to initialize ecosystem composition at the beginning of the simulation period. An important future step will be to use repeat imaging spectrometry measurements to evaluate and improve terrestrial biosphere model predictions of regional and global-scale changes in ecosystem composition.

ACKNOWLEDGEMENTS

This research was supported by funding from NASA HyspIRI Preparatory Activity NNH11ZDA001N-HYSPIRI grant “Linking Terrestrial Biosphere Models with Remote Sensing Measurements of Ecosystem Composition, Structure, and Function”. Logistical support and/or data were provided by the NSF-supported Southern Sierra Critical Zone Observatory. We would like thank Anne Kelly at University of California Irvine for providing forest inventory plots measurements of ecosystem composition at the Southern Sierra CZO flux tower evaluation sites. We also thank Robert Green, Ian McCubbin, Simon Hook, David Thompson and the HyspIRI Airborne Campaign Team for conducting the AVIRIS flights, data and for performing atmospheric correction of the at-sensor reflectance measurements to yield estimates of surface reflectance.

CONFLICT OF INTEREST

We declare no conflicts of interest.

DATA AVAILABILITY STATEMENT

Primary data sharing not applicable to this article as no datasets were generated during the current study. Data that support the findings of this study are appropriately cited within the text in the Section 2. The Ecosystem Demography (ED2.1) terrestrial biosphere model used in this study is available at https://moorcroftlab.oeb.harvard.edu/ed-21, with specific equations used to determine Carbon, Water, and Energy Fluxes in ED2 presented in Appendix 1.

ORCID

Alexander S. Antonarakis https://orcid.org/0000-0003-3194-1682
Paul R. Moorcroft https://orcid.org/0000-0002-2876-4673

REFERENCES

Ahlström, A., Schurgers, G., Arneth, A., & Smith, B. (2012). Robustness and uncertainty in terrestrial ecosystem carbon response to CMIP5 climate change projections. *Environmental Research Letters*, *7*, 044008. https://doi.org/10.1088/1748-9326/7/4/044008

Albani, M., Medvigy, D., Hurtt, G. C., & Moorcroft, P. R. (2006). The contributions of land-use change, CO_2 fertilization, and climate variability to the Eastern US carbon sink. *Global Change Biology*, *12*(12), 2370–2390.

Allen, C. D., Macalady, A. K., Chenchouni, H., Bachelet, D., McDowell, N., Vennetier, M., Kitzberger, T., Rigling, A., Breshears, D. D., Hogg, E. H., Gonzalez, P., Fensham, R., Zhang, Z., Castro, J., Demidova, N., Lim, J.-H., Allard, G., Running, S. W., Semerci, A., & Cobb, N. (2010). A global overview of drought and heat-induced tree mortality reveals emerging climate change risks for forests. *Forest Ecology and Management*, *259*, 660–684. https://doi.org/10.1016/j.foreco.2009.09.001

Antonarakis, A. S., Munger, J. W., & Moorcroft, P. R. (2014). Imaging spectroscopy- and lidar-derived estimates of canopy composition and structure to improve predictions of forest carbon fluxes and ecosystem dynamics. *Geophysical Research Letters*, *41*, 2535–2542. https://doi.org/10.1002/2013GL058373

Antonarakis, A. S., Saatchi, S. S., Chazdon, R. L., & Moorcroft, P. R. (2011). Using Lidar and Radar measurements to constrain predictions of forest ecosystem structure and function. *Ecological Applications*, *21*, 1120–1137. https://doi.org/10.1890/10-0274.1

Asner, G. P., Brodrick, P. G., Anderson, C. B., Vaughn, N., Knapp, D. E., & Martin, R. E. (2016). Progressive forest canopy water loss during the 2012–2015 California drought. *Proceedings of the National Academy of Sciences United States of America*, *113*, E249–E255. https://doi.org/10.1073/pnas.1523397113

Asner, G. P., & Martin, R. E. (2009). Airborne spectranomics: Mapping canopy chemical and taxonomic diversity in tropical forests. *Frontiers in Ecology and the Environment*, *7*, 269–276. https://doi.org/10.1890/070152

Baccini, A., Goetz, S. J., Walker, W. S., Laporte, N. T., Sun, M., Sulla-Menashe, D., Hackler, J., Beck, P. S. A., Dubayah, R., Friedl, M. A., Samanta, S., & Houghton, R. A. (2012). Estimated carbon dioxide emissions from tropical deforestation improved by carbon-density maps. *Nature Climate Change*, *2*, 182–185. https://doi.org/10.1038/nclimate1354

Ball, J. T., Woodrow, I. E., & Berry, J. A. (1986). A model predicting stomatal conductance and its contribution to the control of photosynthesis under different environmental conditions. In I. Biggins (Ed.), *Progress in photosynthesis research* (pp. 221–224). Martinus Nijhoff.

Balster, N. J., & Marshall, J. D. (2000). Decreased needle longevity of fertilized Douglas-fir and grand fir in the northern Rockies. *Tree Physiology*, *20*(17), 1191–1197. https://doi.org/10.1093/treephys/20.17.1191

Bartelink, H. H. (1998). A model of dry matter partitioning in trees. *Tree Physiology*, *18*(2), 91–101. https://doi.org/10.1093/treephys/18.2.91

Berdanier, A. B., & Clark, J. S. (2016). Multiyear drought-induced morbidity preceding tree death in southeastern US forests. *Ecological Applications*, *26*(1), 17–23. https://doi.org/10.1890/15-0274

Berner, L. T., & Law, B. E. (2016). Plant traits, productivity, biomass and soil properties from forest sites in the Pacific Northwest, 1999–2014. *Scientific Data*, *3*(1), 1–14. https://doi.org/10.1038/sdata.2016.2

Bodman, R. W., Rayner, P. J., & Karoly, D. J. (2013). Uncertainty in temperature projections reduced using carbon cycle and climate observations. *Nature Climate Change*, *3*(8), 725–729. https://doi.org/10.1038/nclimate1903

Bogan, S. A., Antonarakis, A. S., & Moorcroft, P. R. (2019). Imaging spectrometry-derived estimates of regional ecosystem composition for the Sierra Nevada, California. *Remote Sensing of Environment*, *228*, 14–30. https://doi.org/10.1016/j.rse.2019.03.031

Bond, B. J., Farnsworth, B. T., Coulombe, R. A., & Winner, W. E. (1999). Foliage physiology and biochemistry in response to light gradients in conifers with varying shade tolerance. *Oecologia*, *120*(2), 183–192. https://doi.org/10.1007/s004420050847

Bontemps, S., Defourny, P., Bogaert, E. V., Arino, O., Kalogirou, V., & Perez, J. R. (2011). *GLOBCOVER 2009-products description and validation report*. European Space Agency.

Byer, S., & Jin, Y. (2017). Detecting drought-induced tree mortality in Sierra Nevada forests with time series of satellite data. *Remote Sensing*, *9*(9), 929. https://doi.org/10.3390/rs9090929

CALVEG. (2010). *Existing vegetation [ESRI Geodatabase]*. USDA-Forest Service, Pacific Southwest Region, (ExistingVegSouthSierra2000_2009_v1).

Campbell, J., Alberti, G., Martin, J., & Law, B. E. (2009). Carbon dynamics of a ponderosa pine plantation following a thinning treatment in the northern Sierra Nevada. *Forest Ecology and Management*, *257*(2), 453–463. https://doi.org/10.1016/j.foreco.2008.09.021

Cawse-Nicholson, K., Townsend, P. A., Schimel, D., Assiri, A. M., Blake, P. L., Buongiorno, M. F., Campbell, P., Carmon, N., Casey, K. A., Correa-Pabón, R. E., Dahlin, K. M., Dashti, H., Dennison, P. E., Dierssen, H., Erickson, A., Fisher, J. B., Frouin, R., Gatebe, C. K., Gholizadeh, H., … Zhang, Q. (2021). NASA's surface biology and geology designated observable: A perspective on surface imaging algorithms. *Remote Sensing of Environment*, *257*, 112349. https://doi.org/10.1016/j.rse.2021.112349

Chojnacky, D. C., Heath, L. S., & Jenkins, J. C. (2014). Updated generalized biomass equations for North American tree species. *Forestry*, *87*(1), 129–151. https://doi.org/10.1093/forestry/cpt053

Clark, J. S., Carpenter, S. R., Barber, M., Collins, S., Dobson, A., Foley, J. A., Lodge, D. M., Pascual, M., Pielke, R., Pizer, W., Pringle, C., Reid, W. V., Rose, K. A., Sala, O., Schlesinger, W. H., Wall, D. H., & Wear, D. (2001). Ecological forecasts: An emerging imperative. *Science*, *293*, 657–660. https://doi.org/10.1126/science.293.5530.657

Clark, M. L., Roberts, D. A., & Clark, D. B. (2005). Hyperspectral discrimination of tropical rain forest tree species at leaf to crown scales. *Remote Sensing of Environment*, *96*, 375–398. https://doi.org/10.1016/j.rse.2005.03.009

Cole, S., & Gray, E. (2015, July 30). *California "Rain Debt" equal to average full year of precipitation*. [NASA Press Release 15-162]. http://www.nasa.gov/press-release/california-rain-debt-equal-to-average-full-year-of-precipitation

Cook, B. I., Ault, T. R., & Smerdon, J. E. (2015). Unprecedented 21st century drought risk in the American Southwest and Central Plains. *Science Advances*, *1*(1), e1400082. https://doi.org/10.1126/sciadv.1400082

Coops, N. C., & Waring, R. H. (2011). A process-based approach to estimate lodgepole pine (*Pinus contorta* Dougl.) distribution in the Pacific Northwest under climate change. *Climatic Change*, *105*(1–2), 313–328.

Dennison, P. E., & Roberts, D. A. (2003a). Endmember selection for multiple endmember spectral mixture analysis using endmember average RSME. *Remote Sensing of Environment*, *87*, 123–135.

Dennison, P. E., & Roberts, D. A. (2003b). The effects of vegetation phenology on endmember selection and species mapping in southern California chaparral. *Remote Sensing of Environment*, *87*, 295–309. https://doi.org/10.1016/j.rse.2003.07.001

Dietze, M. C. (2017). *Ecological forecasting*. Princeton Univ. Press.

Dubayah, R. O., Blair, J. B., Goetz, S., Fatoyinbo, L., Hansen, M., Healey, S., Hofton, M., Hurtt, G., Kellner, J., Luthcke, S., Armston, J., Tang, H., Duncanson, L., Hancock, S., Jantz, P., Marselis, S., Patterson, P. L., Qi, W., & Silva, C. (2020). The global ecosystem dynamics investigation: High-resolution laser ranging of the Earth's forests and topography. *Science of Remote Sensing*, *1*, 100002. https://doi.org/10.1016/j.srs.2020.100002

Dubayah, R. O., & Drake, J. B. (2000). Lidar remote sensing for forestry. *Journal of Forestry*, *98*, 44–46.

Dubayah, R. O., Goetz, S. J., Blair, J. B., Fatoyinbo, T. E., Hansen, M., Healey, S. P., Hofton, M. A., Hurtt, G. C., Kellner, J., Luthcke, S. V., &

Swatantran, A. (2014). *The global ecosystem dynamics investigation*. AGU Fall Meeting Abstracts.

Farquhar, G. D., & Sharkey, T. D. (1982). Stomatal conductance and photosynthesis. *Annual Review of Plant Physiology*, *33*, 317–345.

Farquhar, G. D., von Caemmerer, S., & Berry, J. A. (1980). A biochemical model of photosynthetic CO_2 assimilation in leaves of C3 species. *Planta*, *149*, 78–90. https://doi.org/10.1007/BF00386231

Fisher, J. B., Huntzinger, D. N., Schwalm, C. R., & Sitch, S. (2014). Modeling the terrestrial biosphere. *Annual Review of Environment and Resources*, *39*, 91–123. https://doi.org/10.1146/annurev-environ-012913-093456

Friedl, M. A., Sulla-Menashe, D., Tan, B., Schneider, A., Ramankutty, N., Sibley, A., & Huang, X. (2010). MODIS Collection 5 global land cover: Algorithm refinements and characterization of new datasets. *Remote Sensing of Environment*, *114*, 168–182. https://doi.org/10.1016/j.rse.2009.08.016

Friedlingstein, P., Cox, P., Betts, R., Bopp, L., von Bloh, W., Brovkin, V., Cadule, P., Doney, S., Eby, M., Fung, I., Bala, G., John, J., Jones, C., Joos, F., Kato, T., Kawamiya, M., Knorr, W., Lindsay, K., Matthews, H. D., … Zeng, N. (2006). Climate-carbon cycle feedback analysis: Results from the C4MIP model intercomparison. *Journal of Climate*, *19*, 3337–3353. https://doi.org/10.1175/JCLI3800.1

Friedlingstein, P., Meinshausen, M., Arora, V. K., Jones, C. D., Anav, A., Liddicoat, S. K., & Knutti, R. (2014). Uncertainties in CMIP5 climate projections due to carbon cycle feedbacks. *Journal of Climate*, *27*(2), 511–526. https://doi.org/10.1175/JCLI-D-12-00579.1

Gill, R. A., & Jackson, R. B. (2000). Global patterns of root turnover for terrestrial ecosystems. *New Phytologist*, *147*(1), 13–31. https://doi.org/10.1046/j.1469-8137.2000.00681.x

Goodenough, D. G., Dyk, A., Niemann, K. O., Pearlman, J. S., Chen, H., Han, T., Murdoch, M., & West, C. (2003). Processing hyperion and ALI for forest classification. *IEEE Transactions on Geoscience and Remote Sensing*, *41*, 1321–1331. https://doi.org/10.1109/TGRS.2003.813214

Goulden, M. L., Anderson, R. G., Bales, R. C., Kelly, A. E., Meadows, M., & Winston, G. C. (2012). Evapotranspiration along an elevation gradient in California's Sierra Nevada. *Journal of Geophysical Research: Biogeosciences*, *117*, G03028.

Goulden, M. L., & Bales, R. C. (2014). Mountain runoff vulnerability to increased evapotranspiration with vegetation expansion. *Proceedings of the National Academy of Sciences United States of America*, *111*(39), 14071–14075. https://doi.org/10.1073/pnas.1319316111

Goulden, M. L., & Bales, R. C. (2019). California forest die-off linked to multi-year deep soil drying in 2012–2015 drought. *Nature Geoscience*, *12*(8), 632–637. https://doi.org/10.1038/s41561-019-0388-5

Guanter, L., Kaufmann, H., Segl, K., Foerster, S., Rogass, C., Chabrillat, S., Kuester, T., Hollstein, A., Rossner, G., Chlebek, C., Straif, C., Fischer, S., Schrader, S., Storch, T., Heiden, U., Mueller, A., Bachmann, M., Mühle, H., Müller, R., … Sang, B. (2015). The EnMAP spaceborne imaging spectroscopy mission for earth observation. *Remote Sensing*, *7*(7), 8830–8857. https://doi.org/10.3390/rs70708830

Hancock, S., Armston, J., Hofton, M., Sun, X., Tang, H., Duncanson, L., Kellner, J. R., & Dubayah, R. O. (2019). The GEDI simulator: A large-footprint waveform lidar simulator for calibration and validation of spaceborne missions. *Earth Space Science*, *6*, 294–310. https://doi.org/10.1029/2018EA000506

Heimann, M., Esser, G., Haxeltine, A., Kaduk, J., Kicklighter, D. W., Knorr, W., Kohlmaier, G. H., McGuire, A. D., Melillo, J., Moore, B. III, & Otto, R. D. (1998). Evaluation of terrestrial carbon cycle models through simulations of the seasonal cycle of atmospheric CO_2: First results of a model inter-comparison study. *Global Biogeochemical Cycles*, *12*, 1–24.

Hochberg, E. J., Roberts, D. A., Dennison, P. E., & Hulley, G. C. (2015). Special issue on the Hyperspectral Infrared Imager (HyspIRI): Emerging science in terrestrial and aquatic ecology, radiation balance and hazards. *Remote Sensing of Environment*, *167*, 1–5. https://doi.org/10.1016/j.rse.2015.06.011

Homer, C. G., Dewitz, J. A., Yang, L., Jin, S., Danielson, P., Xian, G., Coulston, J., Herold, N. D., Wickham, J. D., & Megown, K. (2015). Completion of the 2011 National Land Cover Database for the conterminous United States-representing a decade of land cover change information. *Photogrammetric Engineering and Remote Sensing*, *81*, 345–354.

Huntzinger, D. N., Post, W. M., Wei, Y., Michalak, A. M., West, T. O., Jacobson, A. R., Baker, I. T., Chen, J. M., Davis, K. J., Hayes, D. J., Hoffman, F. M., Jain, A. K., Liu, S., McGuire, A. D., Neilson, R. P., Potter, C., Poulter, B., Price, D., Raczka, B. M., … Cook, R. (2012). North American Carbon Program (NACP) regional interim synthesis: Terrestrial biospheric model intercomparison. *Ecological Modelling*, *232*, 144–157. https://doi.org/10.1016/j.ecolmodel.2012.02.004

Hurtt, G. C., Dubayah, R., Drake, J., Moorcroft, P. R., & Fearon, M. (2004). Beyond potential vegetation: Combining Lidar remote sensing and a height-structured ecosystem model for improved carbon stock and flux estimates. *Ecological Applications*, *14*(3), 873–883.

Jenkins, J. C., Chojnacky, D. C., Heath, L. S., & Birdsey, R. A. (2003). National-scale biomass estimators for United States tree species. *Forest Science*, *49*(1), 12–35.

Jetz, W., MacPherson, J., & Guralnik, R. P. (2012). Integrating biodiversity distribution knowledge: Toward a global map of life. *Trends in Ecology and Evolution*, *27*, 151–159. https://doi.org/10.1016/j.tree.2011.09.007

Jung, M., Vetter, M., Herold, M., Churkina, G., Reichstein, M., Zaehle, S., Ciais, P., Viovy, N., Bondeau, A., Chen, Y., Trusilova, K., Feser, F., & Heimann, M. (2007). Uncertainties of modeling gross primary productivity over Europe: A systematic study on the effects of using different drivers and terrestrial biosphere models. *Global Biogeochemical Cycles*, *21*, GB4021. https://doi.org/10.1029/2006GB002915

Karlik, J. F., & McKay, A. H. (2002). Leaf area index, leaf mass density, and allometric relationships derived from harvest of blue oaks in a California oak savanna. In R. B. Standiford, D. McCreary, & K. L. Purcell (Eds.), *Proceedings of the fifth symposium on Oak woodlands: Oaks in California's challenging landscape*. General Technical Report PSW-GTR-184 (pp. 719–729). Pacific Southwest Research Station, Forest Service, US Department of Agriculture.

Kelly, A. E. (2014). *Climate controls on ecosystem production, biomass, and water cycling* [Dissertation, University of California].

Kokaly, R. F., Despain, D. G., Clark, R. N., & Livo, K. E. (2003). Mapping vegetation in Yellowstone National Park using spectral feature analysis of AVIRIS data. *Remote Sensing of Environment*, *84*, 437–456. https://doi.org/10.1016/S0034-4257(02)00133-5

Kolus, H. R., Huntzinger, D. N., Schwalm, C. R., Fisher, J. B., McKay, N., Fang, Y., Michalak, A. M., Schaefer, K., Wei, Y., Poulter, B., Mao, J., Parazoo, N. C., & Shi, X. (2019). Land carbon models underestimate the severity and duration of drought's impact on plant productivity. *Scientific Reports*, *9*(1), 1–10. https://doi.org/10.1038/s41598-019-39373-1

Kozhoridze, G., Orlovsky, N., Orlovsky, L., Blumberg, D. G., & Golan-Goldhirsh, A. (2016). Remote sensing models of structure-related biochemicals and pigments for classification of trees. *Remote Sensing of Environment*, *186*, 184–195. https://doi.org/10.1016/j.rse.2016.08.024

Latham, J., Cumani, R., Rosati, I., & Bloise, M. (2014). *Global land cover SHARE (GLC-SHARE) database beta-release version 1.0*. FAO.

Law, B. E., Sun, O. J., Campbell, J., Van Tuyl, S., & Thornton, P. E. (2003). Changes in carbon storage and fluxes in a chronosequence of ponderosa pine. *Global Change Biology*, *9*(4), 510–524. https://doi.org/10.1046/j.1365-2486.2003.00624.x

Law, B. E., Van Tuyl, S., Cescatti, A., & Baldocchi, D. D. (2001). Estimation of leaf area index in open-canopy ponderosa pine forests at different successional stages and management regimes in Oregon.

Agricultural and Forest Meteorology, *108*(1), 1–14. https://doi.org/10.1016/S0168-1923(01)00226-X

Le Toan, T., Quegan, S., Davidson, M., Balzter, H., Paillou, P., Papathanassiou, K., Plummer, S., Rocca, F., Saatchi, S., Shugart, H., & Ulander, L. (2011). The BIOMASS mission: Mapping global forest biomass to better understand the terrestrial carbon cycle. *Remote Sensing of Environment*, *115*(11), 2850–2860. https://doi.org/10.1016/j.rse.2011.03.020

Lee, C. M., Cable, M. L., Hook, S. J., Green, R. O., Ustin, S. L., Mandl, D. J., & Middleton, E. M. (2015). An introduction to the NASA Hyperspectral InfraRed Imager (HyspIRI) mission and preparatory activities. *Remote Sensing of Environment*, *167*, 6–19. https://doi.org/10.1016/j.rse.2015.06.012

Lefsky, M. A., Harding, D. J., Keller, M., Cohen, W. B., Carabajal, C. C., Del Bom Espirito-Santo, F., Hunter, M. O., & de Oliveira, R. (2005). Estimates of forest canopy height and aboveground biomass using ICESat. *Geophysical Research Letters*, *32*(22), L22S02. https://doi.org/10.1029/2005GL023971

Leuning, R. (1995). A critical appraisal of a combined stomatal-photosynthesis model for C3 plants. *Plant, Cell & Environment*, *18*(4), 339–355.

Longo, M., Knox, R. G., Medvigy, D. M., Levine, N. M., Dietze, M. C., Kim, Y., Swann, A. L., Zhang, K., Rollinson, C. R., Bras, R. L., & Wofsy, S. C. (2019). The biophysics, ecology, and biogeochemistry of functionally diverse, vertically and horizontally heterogeneous ecosystems: The Ecosystem Demography model, version 2.2–Part 1: Model description. *Geoscientific Model Development*, *12*(10), 4309–4346.

Lucas, K. L., & Carter, G. A. (2008). The use of hyperspectral remote sensing to assess vascular plant species richness on Horn Island, Mississippi. *Remote Sensing of Environment*, *112*, 3908–3915. https://doi.org/10.1016/j.rse.2008.06.009

Manter, D. K., & Kerrigan, J. (2004). A/C_i curve analysis across a range of woody plant species: Influence of regression analysis parameters and mesophyll conductance. *Journal of Experimental Botany*, *55*(408), 2581–2588. https://doi.org/10.1093/jxb/erh260

Martin, M. E., Newman, S. D., Aber, J. D., & Congalton, R. G. (1998). Determining forest species composition using high spectral resolution remote sensing data. *Remote Sensing of Environment*, *65*, 249–254. https://doi.org/10.1016/S0034-4257(98)00035-2

Matsunaga, T., Iwasaki, A., Tsuchida, S., Iwao, K., Tanii, J., Kashimura, O., Nakamura, R., Yamamoto, H., Kato, S., Obata, K., Mouri, K., & Tachikawa, T. (2017). Current status of Hyperspectral Imager Suite (HISUI) onboard International Space Station (ISS). *2017 IEEE international geoscience and remote sensing symposium (IGARSS)*. Fort worth, TX, pp. 443–446. https://doi.org/10.1109/IGARSS.2017.8126989

McDowell, N., Pockman, W. T., Allen, C. D., Breshears, D. D., Cobb, N., Kolb, T., Plaut, J., Sperry, J., West, A., Williams, D. G., & Yepez, E. A. (2008). Mechanisms of plant survival and mortality during drought: Why do some plants survive while others succumb to drought? *New Phytologist*, *178*(4), 719–739. https://doi.org/10.1111/j.1469-8137.2008.02436.x

McKelvey, K. S., Skinner, C. N., Chang, C. R., Erman, D. C., Husari, S. J., Parsons, D. J., van Wagtendonk, J. W., & Weatherspoon, C. P. (1996). An overview of fire in the Sierra Nevada. *Sierra Nevada ecosystem project: Final report to congress, vol. II, assessments and scientific basis for management options*: University of California. https://www.fs.fed.us/psw/publications/mckelvey/mckelvey2.PDF

Medvigy, D., & Moorcroft, P. R. (2012). Predicting ecosystem dynamics at regional scales: An evaluation of a terrestrial biosphere model for the forests of northeastern North America. *Philosophical Transactions of the Royal Society B: Biological Sciences*, *367*(1586), 222–235.

Medvigy, D., Wofsy, S. C., Munger, J. W., Hollinger, D. Y., & Moorcroft, P. R. (2009). Mechanistic scaling of ecosystem function and dynamics in space and time: Ecosystem Demography model version 2. *Journal of Geophysical Research*, *114*, G01002. https://doi.org/10.1029/2008JG000812

Michalak, A. M., Jackson, R. B., Marland, G., Sabine, C. L., & The Carbon Cycle Science Working Group. (2011). *A U.S. carbon cycle science plan*. United States Carbon Cycle Carbon Planning.

Miller, C., & Urban, D. L. (1999). A model of surface fire, climate and forest pattern in the Sierra Nevada. *California. Ecological Modelling*, *114*(2–3), 113–135. https://doi.org/10.1016/S0304-3800(98)00119-7

Millikin, C. S., & Bledsoe, C. S. (1999). Biomass and distribution of fine and coarse roots from blue oak (*Quercus douglasii*) trees in the northern Sierra Nevada foothills of California. *Plant and Soil*, *214*(1–2), 27–38.

Misson, L., Panek, J. A., & Goldstein, A. H. (2004). A comparison of three approaches to modeling leaf gas exchange in annually drought-stressed ponderosa pine forests. *Tree Physiology*, *24*(5), 529–541. https://doi.org/10.1093/treephys/24.5.529

Mitchell, K. E., Lohmann, D., Houser, P. R., Wood, E. F., Schaake, J. C., Robock, A., Cosgrove, B. A., Sheffield, J., Duan, Q., Luo, L., & Higgins, R. W. (2004). The multi-institution North American Land Data Assimilation System (NLDAS): Utilizing multiple GCIP products and partners in a continental distributed hydrological modeling system. *Journal of Geophysical Research: Atmospheres*, *109*, D07S90.

Monson, R. K., Sparks, J. P., Rosenstiel, T. N., Scott-Denton, L. E., Huxman, T. E., Harley, P. C., Turnipseed, A. A., Burns, S. P., Backlund, B., & Hu, J. (2005). Climatic influences on net ecosystem CO_2 exchange during the transition from wintertime carbon source to springtime carbon sink in a high-elevation, subalpine forest. *Oecologia*, *146*(1), 130–147. https://doi.org/10.1007/s00442-005-0169-2

Monteith, J. L. (1973). *Principles of environmental physics*. Edward Arnold.

Moorcroft, P. R., Hurtt, G. C., & Pacala, S. W. (2001). A method for scaling vegetation dynamics: The ecosystem demography model (ED). *Ecological Monographs*, *71*(4), 557–585. https://doi.org/10.1890/0012-9615(2001)071[0557:AMFSVD]2.0.CO;2

National Academies of Sciences, Engineering, and Medicine (NASEM). (2018). *Thriving on our changing planet: A decadal strategy for earth observation from space*. The National Academies Press. https://doi.org/10.17226/2493

Natural Resources Conservation Service (NRCS). (2017). *Soil survey geographic (SSURGO) database*. https://websoilsurvey.sc.egov.usda.gov/App/HomePage.htm

O'Geen, A., Safeeq, M., Wagenbrenner, J., Stacy, E., Hartsough, P., Devine, S., Tian, Z., Ferrell, R., Goulden, M., Hopmans, J. W., & Bales, R. (2018). Southern Sierra Critical Zone Observatory and Kings River Experimental Watersheds: A synthesis of measurements, new insights, and future directions. *Vadose Zone Journal*, *17*(1), 1–18. https://doi.org/10.2136/vzj2018.04.0081

Ogle, K., Whitham, T. G., & Cobb, N. S. (2000). Tree-ring variation in pinyon predicts likelihood of death following severe drought. *Ecology*, *81*(11), 3237–3243. https://doi.org/10.1890/0012-9658(2000)081[3237:TRVIPP]2.0.CO;2

Parton, W. J., Schimel, D. S., Cole, C. V., & Ojima, D. S. (1987). Analysis of factors controlling soil organic matter levels in Great Plains grasslands. *Soil Science Society of America Journal*, *51*, 1173–1179. https://doi.org/10.2136/sssaj1987.03615995005100050015x

Paz-Kagan, T., Brodrick, P. G., Vaughn, N. R., Das, A. J., Stephenson, N. L., Nydick, K. R., & Asner, G. P. (2017). What mediates tree mortality during drought in the southern Sierra Nevada? *Ecological Applications*, *27*(8), 2443–2457. https://doi.org/10.1002/eap.1620

Potter, C. S. (2016). Landsat image analysis of tree mortality in the Southern Sierra Nevada region of California during the 2013–2015 drought. *Journal of Earth Science & Climatic Change*, *7*, 342. https://doi.org/10.4172/2157-7617.1000342

Poulter, B., MacBean, N., Hartley, A., Khlystova, I., Arino, O., Betts, R., Bontemps, S., Boettcher, M., Brockmann, C., Defourny, P., Hagemann, S., Herold, M., Kirches, G., Lamarche, C., Lederer, D., Ottlé, C., Peters, M., & Peylin, P. (2015). Plant functional type classification for earth system models: Results from the European Space Agency's Land Cover Climate Change Initiative. *Geoscientific Model Development*, *8*, 2315–2328. https://doi.org/10.5194/gmd-8-2315-2015

Quaife, T., Quegan, S., Disney, M., Lewis, P., Lomas, M., & Woodward, F. I. (2008). Impact of land cover uncertainties on estimates of biospheric carbon fluxes. *Global Biogeochemical Cycles*, *22*, 1–12. https://doi.org/10.1029/2007GB003097

Restaino, C., Young, D. J., Estes, B., Gross, S., Wuenschel, A., Meyer, M., & Safford, H. (2019). Forest structure and climate mediate drought-induced tree mortality in forests of the Sierra Nevada, USA. *Ecological Applications*, *29*(4), e01902.

Roberts, D. A., Gardner, M. E., Church, R., Ustin, S. L., & Green, R. O. (1997). Optimum strategies for mapping vegetation using multiple-endmember spectral mixture models. *Proceedings SPIE 3118, Imaging Spectrometry III*, https://doi.org/10.1117/12.278930

Roberts, D. A., Gardner, M., Church, R., Ustin, S., Scheer, G., & Green, R. O. (1998). Mapping Chaparral in the Santa Monica Mountains using multiple endmember spectral mixture models. *Remote Sensing of Environment*, *65*, 267–279. https://doi.org/10.1016/S0034-4257(98)00037-6

Robeson, S. M. (2015). Revisiting the recent California drought as an extreme value. *Geophysical Research Letters*, *42*(16), 6771–6779. https://doi.org/10.1002/2015GL064593

Rosen, P. A., Hensley, S., Shaffer, S., Veilleux, L., Chakraborty, M., Misra, T., Bhan, R., Raju Sagi, V., & Satish, R. (2015). The NASA-ISRO SAR mission: An international space partnership for science and societal benefit. *IEEE Radar Conference (Radar Conference)*, 1610–1613.

Roth, K. L., Dennison, P. E., & Roberts, D. A. (2012). Comparing endmember selection techniques for accurate mapping of plant species and land cover using imaging spectrometer data. *Remote Sensing of Environment*, *127*, 139–152. https://doi.org/10.1016/j.rse.2012.08.030

Roth, K. L., Roberts, D. A., Dennison, P. E., Alonzo, M., Peterson, S. H., & Beland, M. (2015). Differentiating plant species within and across diverse ecosystems with imaging spectroscopy. *Remote Sensing of Environment*, *167*, 135–151. https://doi.org/10.1016/j.rse.2015.05.007

Saatchi, S. S., Harris, N. L., Brown, S., Lefsky, M., Mitchard, E. T. A., Salas, W., Zutta, B. R., Buermann, W., Lewis, S. L., Hagen, S., Petrova, S., White, L., Silman, M., & Morel, A. (2011). Benchmark map of forest carbon stocks in tropical regions across three continents. *Proceedings of the National Academy of Sciences United States of America*, *108*(24), 9899–9904. https://doi.org/10.1073/pnas.1019576108

Saatchi, S. S., Houghton, R. A., Dos Santos Alvala, R. C., Soares, J. V., & Yu, Y. (2007). Distribution of aboveground live biomass in the Amazon. *Global Change Biology*, *13*, 816–837.

Schaefer, K., Schwalm, C. R., Williams, C., Arain, M. A., Barr, A., Chen, J. M., Davis, K. J., Dimitrov, D., Hilton, T. W., Hollinger, D. Y., Humphreys, E., Poulter, B., Raczka, B. M., Richardson, A. D., Sahoo, A., Thornton, P., Vargas, R., Verbeeck, H., Anderson, R., … Zhou, X. (2012). A model-data comparison of gross primary productivity: Results from the North American Carbon Program site synthesis. *Journal of Geophysical Research: Biogeosciences*, *117*(G3), G03010. https://doi.org/10.1029/2012JG001960

Schimel, D. S., Asner, G. P., & Moorcroft, P. R. (2013). Observing changing ecological diversity in the Anthropocene. *Frontiers in Ecology and the Environment*, *11*, 129–137. https://doi.org/10.1890/120111

Schnabel, S., Dahlgren, R. A., & Moreno-Marcos, G. (2013). Soil and water dynamics. In P. Campos, L. Huntsinger, J. L. Oviedo, P. F. Starrs, M. Diaz, R. B. Standiford, & G. Montero (Eds.), *Mediterranean oak woodland working landscapes* (pp. 91–121). Springer.

Schwalm, C. R., Williams, C. A., Schaefer, K., Anderson, R., Arain, M. A., Baker, I., Barr, A., Black, T. A., Chen, G., Chen, J. M., & Ciais, P. (2010). A model-data intercomparison of CO_2 exchange across North America: Results from the North American Carbon Program site synthesis. *Journal of Geophysical Research: Biogeosciences*, *115*(G3), G00H05.

Schwartz, M. W., Butt, N., Dolanc, C. R., Holguin, A., Moritz, M. A., North, M. P., Safford, H. D., Stephenson, N. L., Thorne, J. H., & van Mantgem, P. J. (2015). Increasing elevation of fire in the Sierra Nevada and implications for forest change. *Ecosphere*, *6*(7), 1–10. https://doi.org/10.1890/ES15-00003.1

Somers, B., & Asner, G. P. (2013). Invasive species mapping in Hawaiian rainforests using multi-temporal Hyperion spaceborne imaging spectroscopy. *IEEE Journal of Selected Topics in Applied Earth Observations and Remote Sensing*, *6*(2), 351–359. https://doi.org/10.1109/JSTARS.2012.2203796

Southern Sierra CZO. (2012). *KREW quantitative soil pits*. https://eng.ucmerced.edu/snsjho/files/MHWG/Field/Southern_Sierra_CZO_KREW

Sterling, S., & Ducharne, A. (2008). Comprehensive data set of global land cover change for land surface model applications. *Global Biogeochemical Cycles*, *22*(3), GB3017. https://doi.org/10.1029/2007GB002959

Swain, D. L., Langenbrunner, B., Neelin, J. D., & Hall, A. (2018). Increasing precipitation volatility in twenty-first-century California. *Nature Climate Change*, *8*(5), 427–433. https://doi.org/10.1038/s41558-018-0140-y

Taylor, A. H., Trouet, V., Skinner, C. N., & Stephens, S. (2016). Socioecological transitions trigger fire regime shifts and modulate fire–climate interactions in the Sierra Nevada, USA, 1600–2015 CE. *Proceedings of the National Academy of Sciences United States of America*, *113*, 13684–13689. https://doi.org/10.1073/pnas.1609775113

Ter-Mikaelian, M. T., & Korzukhin, M. D. (1997). Biomass equations for sixty-five North American tree species. *Forest Ecology and Management*, *97*(1), 1–24. https://doi.org/10.1016/S0378-1127(97)00019-4

Thomas, Q. R., Hurtt, G. C., Dubayah, R., & Schilz, M. H. (2008). Using lidar data and a height-structured ecosystem model to estimate forest carbon stocks and fluxes over mountainous terrain. *Canadian Journal of Remote Sensing*, *34*, S351–S363. https://doi.org/10.5589/m08-036

Thompson, D. R., Gao, B.-C., Green, R. O., Roberts, D. A., Dennison, P. E., & Lundeen, S. R. (2015). Atmospheric correction for global mapping spectroscopy: ATREM advances for the HyspIRI preparatory campaign. *Remote Sensing of Environment*, *167*, 64–77. https://doi.org/10.1016/j.rse.2015.02.010

Tingey, D. T., Phillips, D. L., Johnson, M. G., Rygiewicz, P. T., Beedlow, P. A., & Hogsett, W. E. (2005). Estimates of Douglas-fir fine root production and mortality from minirhizotrons. *Forest Ecology and Management*, *204*(2–3), 359–370. https://doi.org/10.1016/j.foreco.2004.09.010

Treuhaft, R. N., Chapman, B. D., Dos Sãntos, J. R., Gonçalves, F. G., Dutra, L. V., Graça, P. M. L. A. D., & Drake, J. B. (2009). Vegetation profiles in tropical forests from multibaseline interferometric synthetic aperture radar, field, and lidar measurements. *Journal of Geophysical Research: Atmospheres*, *114*(D23), D23110.

USFS. (2015). *2015 Forest health protection arial detection survey*. www.fs.usda.gov/detail/r5/forest-grasslandhealth/http://www.takepart.com/article/2016/06/22/california-worse-millions-more-trees-gone

von Caemmerer, S., & Farquhar, G. D. (1981). Some relationships between the biochemistry of photosynthesis and the gas exchange of leaves. *Planta*, *153*, 376–387. https://doi.org/10.1007/BF00384257

Warren, C. R., Livingston, N. J., & Turpin, D. H. (2004). Water stress decreases the transfer conductance of Douglas-fir (*Pseudotsuga menziesii*) seedlings. *Tree Physiology*, *24*(9), 971–979.

Wehr, R., Commane, R., Munger, J. W., McManus, J. B., Nelson, D. D., Zahniser, M. S., Saleska, S. R., & Wofsy, S. C. (2017). Dynamics of canopy stomatal conductance, transpiration, and evaporation in a temperate deciduous forest, validated by carbonyl sulfide uptake. *Biogeosciences*, *14*(2), 389–401. https://doi.org/10.5194/bg-14-389-2017

Xu, L., & Baldocchi, D. D. (2003). Seasonal trends in photosynthetic parameters and stomatal conductance of blue oak (*Quercus douglasii*) under prolonged summer drought and high temperature. *Tree Physiology*, *23*(13), 865–877. https://doi.org/10.1093/treephys/23.13.865

Xu, L., Baldocchi, D. D., & Tang, J. (2004). How soil moisture, rain pulses, and growth alter the response of ecosystem respiration to temperature. *Global Biogeochemical Cycles*, *18*(4), GB4002. https://doi.org/10.1029/2004GB002281

Xu, X., Medvigy, D., Powers, J. S., Becknell, J. M., & Guan, K. (2016). Diversity in plant hydraulic traits explains seasonal and inter-annual variations of vegetation dynamics in seasonally dry tropical forests. *New Phytologist*, *212*(1), 80–95. https://doi.org/10.1111/nph.14009

Young, D. J., Stevens, J. T., Earles, J. M., Moore, J., Ellis, A., Jirka, A. L., & Latimer, A. M. (2017). Long-term climate and competition explain forest mortality patterns under extreme drought. *Ecology Letters*, *20*(1), 78–86. https://doi.org/10.1111/ele.12711

Zhang, J., Rivard, B., Sánchez-Azofeifa, A., & Castro- Esau, C. (2006). Intra- and inter-class spectral variability of tropical tree species at La Selva, Costa Rica: Implications for species identification using HYDICE imagery. *Remote Sensing of Environment*, *105*, 129–141. https://doi.org/10.1016/j.rse.2006.06.010

Zhang, K., Almeida Castanho, A. D., Galbraith, D. R., Moghim, S., Levine, N. M., Bras, R. L., Coe, M. T., Costa, M. H., Malhi, Y., Longo, M., & Knox, R. G. (2015). The fate of Amazonian ecosystems over the coming century arising from changes in climate, atmospheric CO_2, and land use. *Global Change Biology*, *21*(7), 2569–2587.

Zhang, X., Friedl, M. A., Schaaf, C. B., Strahler, A. H., Hodges, J. C., Gao, F., Reed, B. C., & Huete, A. (2003). Monitoring vegetation phenology using MODIS. *Remote Sensing of Environment*, *84*, 471–475. https://doi.org/10.1016/S0034-4257(02)00135-9

SUPPORTING INFORMATION

Additional supporting information may be found in the online version of the article at the publisher's website.

How to cite this article: Antonarakis, A. S., Bogan, S. A., Goulden, M. L., & Moorcroft, P. R. (2022). Impacts of the 2012–2015 Californian drought on carbon, water and energy fluxes in the Californian Sierras: Results from an imaging spectrometry-constrained terrestrial biosphere model. *Global Change Biology*, 28, 1823–1852. https://doi.org/10.1111/gcb.15995

APPENDIX 1

CARBON, WATER AND ENERGY FLUXES IN ED2

The ecosystem productivity (NEP) of the ecosystem is defined as the integral of the per plant net primary productivity (NPP) integrated over all plants within the grid cell, minus the heterotrophic respiration, r_h:

$$\text{Canopy NEP} = \int_a \left(\int_z \left(\text{NPP}^{(i)}(z,a) \right) * n^i(z,a)\,dz - r_h(a) \right) p(a)\,da \qquad \text{(A1)}$$

where n^i and p are defined as plant density of plant functional type i and distribution of gap ages, respectively. Carbon fluxes in Equation (A1) are calculated on a per-plant basis using the model of leaf-level carbon assimilation and water fluxes developed by Farquhar, Ball, Berry and others (Ball et al., 1986; Farquhar et al., 1980; Farquhar & Sharkey, 1982; von Caemmerer & Farquhar, 1981).

The instantaneous rates of net photosynthesis (A_{net}) and evapotranspiration (ET) (Ψ_{net}) are influenced by water availability. Photosynthesis and ET are taken to be linear combinations of their rates under conditions of open (A_o Ψ_o) and closed (A_c Ψ_c) stomata, the weighting of being determined by a plant's water availability relative to its overall water demand:

$$A_{net} = f_{o,w} A_o + \left(1 - f_{o,w}\right) A_c \qquad \text{(A2)}$$

$$\Psi_{net} = f_{o,w} \Psi_o + \left(1 - f_{o,w}\right) \Psi_c \qquad \text{(A3)}$$

where the open stomata weighting is given as a function of the plants water demand and the water availability:

$$f_{o,w} = \frac{1}{1 + \frac{\text{Demand}}{\text{Supply}}}, \ \text{Demand} = \Psi_o \text{SLA} \cdot B_{leaf}, \text{Supply} = K_w W_{avail,tot} B_{root} \qquad \text{(A4)}$$

where SLA is the plant's specific leaf area, B_{leaf} is the plant's leaf biomass, $W_{avail,tot}$ is the total amount of water accessible to the plant, given its rooting depth B_{root} is the plant's root biomass and K_w is the conductivity of water and is a constant. The leaf-level demand of photosynthesis is given by:

$$A_o = \min\left(J_e, J_c\right) - \gamma V_m\left(T_v\right) \ \text{for open stomata}$$

$$A_o = -\gamma V_m\left(T_v\right) \ \text{for closed stomata} \qquad \text{(A5)}$$

where γV_m represents leaf respiration at the plant level, $V_m\left(T_v\right)$ is the maximum capacity of Rubisco to perform the carboxylase function at a given temperature and γ is proportionality constant. In the fall, photosynthesis is ramped down according to the available active leaf area, or phenology. The light limited (J_e) and Rubisco limited (J_c) rate of photosynthesis is given by:

$$J_e = \alpha \text{PAR}_v \frac{C_{inter} - \Gamma}{C_{inter} + 2\Gamma} \ \text{and} \ J_c = \frac{V_m\left(T_v\right)\left(C_{inter} - \Gamma\right)}{C_{inter} + K_1\left(1 + K_2\right)} \qquad \text{(A6)}$$

where α is the quantum efficiency, PAR_v is the PAR absorbed by the vegetation layer, C_{inter} is the intercellular CO_2 concentration, and Γ is the compensation point for gross photosynthesis directly related to the temperature, and K_1 and K_2 are the Michaelis–Menten coefficients for CO_2 and O_2, respectively. The intercellular boundary layer is directly related to the boundary mixing ratios for H_2O and CO_2 following Monteith (1973) and Leuning et al. (1995):

$$C_{inter} = C_S - \frac{A_o}{1.6 g_{sw}} \ \text{and} \ e_L = e_S + \frac{\Psi_o}{g_{sw}} \qquad \text{(A7)}$$

where g_{sw} is the stomatal conductance for water dependent on whether the stomata are open or closed, C_S and e_S are the CO_2 and H_2O concentrations within the leaf boundary layer both related to the boundary layer conductance of water from free and forced convection.

The plant level NPP is then calculated as:

$$\mathrm{NPP}^{(i)}(z,a) = A_{\mathrm{NET}}\,\mathrm{SLA}^{i} B_{\mathrm{leaf}}{}^{i} - \beta_{\mathrm{root}} B_{\mathrm{root}}{}^{i} - \beta_{\mathrm{storage}}\, B_{\mathrm{storage}}{}^{i} \quad \text{(A8)}$$

where B_{root} and B_{storage} are the size of the plant's fine-root and storage carbon pools and β_{root} and β_{storage} are their respiration rates per unit mass.

The decomposition fluxes (r_h) are based on the model of Parton et al. (1987). The process described here is at the per area level. For fast pool decomposition:

$$F_{\mathrm{f,decomp}} = A\, k_2 C_{\mathrm{f}} \quad \text{(A9)}$$

where k_2 is a rate constant defining the fast carbon pool (C_f) and A is the product of two functions $f(x_w)$ and $f(T)$ whose values vary between 0 and 1, that, respectively, account for the temperature and moisture dependence of heterotrophic respiration. The moisture dependency $f(x_w)$ is given as:

$$f\left(x_W\right) = \begin{cases} exp\left[\left(x_W - W_{\mathrm{opt}}\right) w_1\right] & x_W < W_{\mathrm{opt}} \\ exp\left[\left(W_{\mathrm{opt}} - x_W\right) w_2\right] & x_W > W_{\mathrm{opt}} \end{cases} \quad \text{(A10)}$$

and the temperature dependence of A is given as:

$$f(T) = \exp\left[\frac{\log Q_{10}}{10}\left(T - 318.15\right)\right] \quad \text{(A11)}$$

where x_W is the soil moisture, W_{opt} is the optimum soil moisture for decomposition, w_1 and w_2 are shape parameters for the moisture dependence of heterotrophic respiration, Q_{10} determines the response of decomposition to soil temperature and T is the temperature in Kelvin. The structural pool decomposition flux is defined as:

$$F_{\mathrm{st,decomp}} = A L_c k_1 C_{\mathrm{s,struct}} f_{\mathrm{std}} \quad \text{(A12)}$$

Here, k_1 is a rate constant setting the residence time of the structural pool $C_{\mathrm{s,struct}}$, and L_c is the amount of lignin transferred out of the structural pool. Finally, the slow pool has a decomposition rate of:

$$F_{\mathrm{sl,decomp}} = A k_3 C_{\mathrm{s,slow}} \quad \text{(A13)}$$

The net decomposition rate or total heterotrophic respiration is given by:

$$r_h = F_{\mathrm{f,decomp}} + F_{\mathrm{st,decomp}} + F_{\mathrm{sl,decomp}} \quad \text{(A14)}$$

APPENDIX 2

CHANGES IN SENSIBLE HEAT FLUXES

Regional patterns of predicted sensible heat fluxes are shown in Figure S8. In 2010 and 2011, prior to the onset of the drought, at low- to mid-elevations (<2000 m), the spatial pattern of sensible heat (Figure S8a,b) is relatively uniform varying between 45 and 50 W m^{-2}. At higher elevations (above 2000 m), sensible heat is more variable with fluxes of <35 W m^{-2} in the areas of bare rock that are found in the northern parts of transect, but higher sensible heat fluxes of >55 W m^{-2} in high-elevation forested areas (compare Figure 4 and Figure S8b).

Coincident with the large declines in transpiration and evaporation described earlier (see Figure 10), following the onset of the drought, sensible heat flux (H) increases across the region by 52% from 46 to 70 W m^{-2}. As would be expected given the larger declines in transpiration that occur at mid-elevations (1000–2200 m; Figure 10a,b), mid-elevation H increases by 60% from 45.5 to 73 W m^{-2}, whereas at low-elevations <1000 m H increases by 45% from 47.75 to 69.2 W m^{-2}. At higher elevations (above 2000 m) sensible heat in the areas of bare rock that are found in the northern parts of transect increases by 80% from 38.5 to 69.5 W m^{-2}, with high-elevation forested areas increasing by 45%–50% similar to low elevation increases.

APPENDIX 3

SOURCES OF ERROR IN THE REGIONAL SIMULATIONS

The impacts of the regional composition and structure estimates on the accuracy the of regional predictions of carbon and water fluxes was assessed at the four flux tower sites by comparing the model's GPP, NEP and ET predictions between simulations forced with observed site-level meteorology (OBS), and initialized with either: (i) site-level ground-based measurements of structure, (ii) imaging spectrometry-based composition and site-level ground-based measurements of structure; or (iii) imaging spectrometry-based composition and FIA-based structure. As seen in Figure S6, the seasonal patterns of carbon and water fluxes obtained from these different estimates of ecosystem composition and structure are generally similar (compare pink, blue and red lines, respectively). Close examination of GPP seasonality (Figure S6e–h) shows that use of the imaging spectrometry-based composition and FIA-based estimates of structure (IS:FIA:OBS, pink lines) compared with imaging spectrometry-based composition and ground-based estimates of structure (IS:GND:OBS, blue lines) and ground-based initialization (GND:GND:OBS, red lines), results in lower peaks in summertime GPP at SJER, and higher summertime peaks in GPP at P301 and Shorthair. These differences in summertime GPP are also reflected in lower (SJER) or higher (P301 and Shorthair) peaks in summertime NEP (Figure S6i–l). Similarly, differences in water fluxes between the simulations were small (Figure S6m–p).

Simulations with imaging spectrometry-based composition and ground-based structure (IS:GND:OBS, blue lines) marginally increased summertime ET compared with ground-based initialization (GND:GND:OBS, red lines), whereas the simulations with imaging spectrometry-based composition and FIA-based estimates of structure (IS:FIA:OBS, pink lines) had marginally lower summertime ET peaks. However, in all three simulations the seasonality of ET was offset from the observations: the summertime peaks in ET occurred 1-month in advance of observations at SJER, Soaproot and P301, and 2 months in advance at Shorthair (blue, red and pink lines in Figure S6m–p).

Comparison of the incremental changes in the root-mean-squared deviations (RMSDs) of the annual GPP, NEP and ET predictions between the simulation configurations (i)-(iii) described above indicates only small differences in the predictions between the simulations (Table S1). The root mean square error (RMSE) ranges for GPP, NEP and ET predictions of the ground-based initialization (GND:GND:OBS) were 0.019–0.028 kgC m^{-2} $month^{-1}$, 0.022–0.028 kgC m^{-2} $month^{-1}$, and 19–29 mm $month^{-1}$, respectively (Table S1). Replacing the ground-based composition with the imaging spectrometry-based composition estimate (i.e. IS:GND:OBS vs. GND:GND:OBS) yielded GPP RMSDs of 0.002–0.009 kgC m^{-2} $month^{-1}$ and NEP RMSDs of 0.002–0.010 kgC m^{-2} $month^{-1}$ (Table S1). Replacing the ground-based estimate of structure with FIA-based structure (i.e. IS:FIA:OBS vs. IS:GND:OBS) resulted in generally higher RMSDs (GPP: 0.007–0.014 kgC m^{-2} $month^{-1}$; NEP 0.004–0.012 kgC m^{-2} $month^{-1}$; ET 3–9 mm $month^{-1}$ Table S1).

In a similar manner, we assessed the impacts of the regional meteorological forcing on the accuracy of the model's predictions by comparing simulations at the four flux tower sites initialized with imaging spectrometry-based composition and FIA-based structure forced with the NLDAS regional meteorology to equivalent simulations forced with the observed meteorological available at these sites. The use of NLDAS forcing increased the error in carbon flux predictions most notably during the summer and autumn months of 2012–2014 at Soaproot and P301 [Figure S6, compare green and pink lines, respectively, in panels (e–h; GPP) and panels (i–l; NEP)]. Compared with the initializations with observed meteorology (IS:FIA:OBS), the simulations with regional meteorology (IS:FIA:NLDAS) resulted in annual GPP RMSDs of 0.010, 0.041, 0.040 and 0.014 kgC m^{-2} $month^{-1}$ and NEP RMSDs 0.012, 0.031, 0.042 and 0.015 kgC m^{-2} $month^{-1}$ at SJER, Soaproot, P301, and Shorthair, respectively (Table S1). This also resulted in higher RMSDs for annual ET of 19, 23, 23 and 13 mm $month^{-1}$ at SJER, Soaproot, P301 and Shorthair, respectively, compared with equivalent initializations with observed meteorology (Table S1).